

# Mixed Convection From an Isothermal Rough Plate

Aubrey G. Jaffer and Martin S. Jaffer

e-mail: agj@alum.mit.edu

## Abstract

This investigation derives formulas to predict the mixed convective surface conductance of a flat isotropic surface roughness having a convex perimeter in a Newtonian fluid with a steady forced flow in the plane of that roughness.

Heat transfer measurements of a 30.5 cm square rough plate with forced air velocities between 0.1 m/s and 2.5 m/s were made by the present apparatus in two inclined and all five orthogonal orientations. The present work's formulas are compared with 104 measurements in twelve data-sets. The twelve data-sets have root-mean-square relative error (RMSRE) values between 1.3% and 4% relative to the present theory.

The present work's formulas are also compared with 78 measurements in 28 data-sets on five vertical rough surfaces in horizontal flow from Rowley, Algren, and Blackshaw (1930). The five stucco data-sets have RMSRE values between 2.5% and 6.5%; the other data-sets have RMSRE values between 0.2% and 5%.

This research did not receive any specific grant from funding agencies in the public, commercial, or not-for-profit sectors.

## Table of Contents

1. <i>Introduction</i> .....	2
2. <i>Natural Convection</i> .....	5
3. <i>Forced Convection</i> .....	7
4. <i>Mixing Natural and Forced Convections</i> .....	9
5. <i>Horizontal Forced Flow</i> .....	10
6. <i>Vertical Plate With Vertical Forced Flow</i> .....	15
7. <i>Vertical Plate With Forced Flows at any Angle</i> .....	18
8. <i>Mixed Convection From an Inclined Plate</i> .....	19
9. <i>Practice</i> .....	20
10. <i>Results</i> .....	21
11. <i>Discussion</i> .....	22
12. <i>Conclusions</i> .....	23
13. <i>Nomenclature</i> .....	23
14. <i>Appendix A: Velocity Profiles</i> .....	25
15. <i>Appendix B: Plateau Islands Roughness Correction</i> .....	26
16. <i>Appendix C: Apparatus and Measurement Methodology</i> .....	27
17. <i>References</i> .....	37

## 1. Introduction

Natural convection is the flow caused by nonuniform density in a fluid under the influence of gravity. Forced convection is the heat or solute transfer to or from a surface induced by forced fluid flow parallel to that surface. Mixed convection is the heat or solute transfer when both processes are operating simultaneously.

Modeling mixed convection from the exterior faces of walls and roofs is essential to predicting the thermal performance of buildings and determining their heating and cooling requirements. This investigation derives and tests mixed convection formulas for a rough, flat exterior face at any inclination, subjected to forced flow in the plane of the surface.

Three modes of forced flow of a Newtonian fluid along a (flat) surface are laminar flow, turbulent flow, and rough flow. Flow along flat, smooth plates gradually transitions from laminar to turbulent in a continuous boundary-layer<sup>1</sup> (Lienhard [1]).

Surface roughness repeatedly disrupts the boundary-layer in rough flow, which occurs along rough surfaces (Jaffer [2]).

Forced convection fluid flow is parallel to the surface. In natural convection the temperature difference between the fluid and surface creates an upward or downward fluid flow, which is not necessarily parallel to the surface. Along a vertical plate, “aiding” has natural and forced flows in the same direction; “opposing” flows are in opposite directions.

Natural convection is sensitive to plate inclination, while forced convection is not. Forced convection has different formulas for laminar, turbulent, and rough flows, while a single formula governs both laminar and turbulent natural convection (Fujii and Imura [3], Churchill and Chu [4], Jaffer [5]).

There is a symmetry in external natural convection; a cooled plate induces downward flow instead of upward flow. Flow from a cooled upper face is the mirror image of flow from a heated lower face. Flow from a cooled lower face is the mirror image of flow from a heated upper face.

The rest of this investigation assumes a surface warmer than the fluid.

**1.1 Fluid Mechanics.** In engineering, heat transfer rates for both natural and forced convection are expressed using the average surface conductance  $\bar{h}$  with units  $\text{W}/(\text{m}^2 \cdot \text{K})$ .

In fluid mechanics, the convective heat transfer rate is represented by the dimensionless average Nusselt number ( $\overline{Nu} \equiv \bar{h} L/k$ ), where  $k$  is the fluid’s thermal conductivity with units  $\text{W}/(\text{m} \cdot \text{K})$ , and  $L$  is the system’s characteristic length (m).

The Reynolds number  $Re$  is dimensionless and proportional to fluid velocity. The Rayleigh number  $Ra$  is the impetus for fluid flow due to temperature difference and gravity. A fluid’s Prandtl number  $Pr$  is its momentum diffusivity per thermal diffusivity ratio. The system’s characteristic length  $L$  scales both  $\overline{Nu}$  and  $Re$ ;  $Ra$  is scaled by  $L^3$ ; both  $\bar{h}$  and  $Pr$  are independent of  $L$ .

**1.2 Combining Transfer Processes.** Formula (1) is an unnamed form for combining functions which appears frequently in heat transfer formulas:

$$F^p = F_1^p + F_2^p \quad (1)$$

Churchill and Usagi [6] stated that such formulas are “remarkably successful in correlating rates of transfer for processes which vary uniformly between these limiting cases.” Convection transfers heat (or solute) between the plate and fluid.

**1.3 The  $\ell^p$ -norm.** When  $F_1 \geq 0$  and  $F_2 \geq 0$ , taking the  $p$ th root of both sides of Equation (1) yields a vector-space functional form known as the  $\ell^p$ -norm, which is notated  $\|F_1, F_2\|_p$ :

$$\|F_1, F_2\|_p \equiv [ |F_1|^p + |F_2|^p ]^{1/p} \quad (2)$$

Norms generalize the notion of distance. Formally, a vector-space norm obeys the triangle inequality:  $\|F_1, F_2\|_p \leq |F_1| + |F_2|$ , which holds only for  $p \geq 1$ . However,  $p < 1$  is also useful.

---

<sup>1</sup> Schlichting [7] describes a boundary-layer: “In that thin layer the velocity of the fluid increases from zero at the wall (no slip) to its full value which corresponds to external frictionless flow.”

- When  $p > 1$ , the processes modeled by  $F_1$  and  $F_2$  compete and  $\|F_1, F_2\|_p \geq \max(|F_1|, |F_2|)$ ; the most competitive case is  $\|F_1, F_2\|_{+\infty} \equiv \max(|F_1|, |F_2|)$ .
  - Formula (25) uses the  $\ell^3$ -norm.
  - Formula (26) uses the  $\ell^{\sqrt{3}}$ -norm.
- The  $\ell^2$ -norm is equivalent to root-sum-squared; it models perpendicular competitive processes.
  - Formulas (21) and (23) use the  $\ell^2$ -norm.
- The  $\ell^1$ -norm models independent processes;  $\|F_1, F_2\|_1 \equiv |F_1| + |F_2|$ .
- When  $0 < p < 1$ , the processes cooperate and  $\|F_1, F_2\|_p \geq |F_1| + |F_2|$ .
  - Cooperation between conduction and flow-induced heat transfer manifests as the  $\ell^{1/2}$ -norm in natural convection Formula (7).
- When  $p < 0$ ,  $\|F_1, F_2\|_p \leq \min(|F_1|, |F_2|)$ , with the transition sharpness controlled by  $p$ ; the extreme case is  $\|F_1, F_2\|_{-\infty} \equiv \min(|F_1|, |F_2|)$ . Negative  $p$  can model a single flow through serial processes; the most restrictive process limits the flow.
  - Formula (18) uses the  $\ell^{-4}$ -norm.
  - Formula (41) uses the  $\ell^{-\sqrt{1/3}}$ -norm.

**1.4 Roughness.** The present theory treats surface roughness as an elevation function  $z(x, y)$  defined on an area  $A$  having a convex perimeter. Function  $z(x, y)$  has only one value at each  $(x, y)$  coordinate; thus surfaces with tunnels and overhangs are disqualified, as are porous surfaces. The mean elevation  $\bar{z}$  and root-mean-squared (RMS) height-of-roughness  $\varepsilon \ll L$  are:

$$\bar{z} = \frac{\int_A z \, dA}{\int_A dA} \quad (3)$$

$$\varepsilon = \sqrt{\frac{\int_A |z - \bar{z}|^2 \, dA}{\int_A dA}} \quad (4)$$

### 1.5 Prior Work.

Nearly all of the experimental prior works ([8, 9, 10, 11, 12, 13, 14]) concern smooth plates. The exception is Rowley, Algren, and Blackshaw [15], the 1930 result of cooperative research between the University of Minnesota and the American Society of Heating and Ventilation Engineers. They measured mixed convection of 0.305 m square vertical plates in horizontal flow in a wind tunnel. They tested common rough exterior surfaces, specifically concrete, brick, stucco, and rough and smooth plaster.

Mixed convection measurements from the graphs in Rowley et al. [15] were captured by measuring the distance from each point to its graph's axes, then scaling to the graph's units using the “Engauge” software (version 12.1). Table 1 lists the data-sets to be compared with the present theory, where  $\theta$  is the angle of the plate from vertical and  $\psi$  is the angle of the forced flow from the zenith;  $\psi = 90^\circ$  is horizontal.

**1.6 Present Apparatus.** The present apparatus combines an open intake wind-tunnel, software phase-locked loop fan control, and a heated aluminum plate centered in the test chamber by a six wire suspension.

This apparatus measured average mixed convection in air with  $2300 < Re_F < 93000$ , a 40:1 range. The wind-tunnel chassis (1.3 m  $\times$  0.61 m  $\times$  0.65 m) was small enough to allow positioning in horizontal, vertical, and inclined orientations. Section 16 describes the apparatus and measurement methodology.

**1.7 Approaches.** Rowley et al. [15] provided graphs for engineering use which cover both laminar and turbulent flows. It applies only to forced horizontal flow in the plane of a vertical plate. It lacked a roughness metric which would have allowed application to other types of rough surfaces. Unfortunately, forced convection from rough plates does not scale simply, being inversely proportional to  $\log^2(L/\varepsilon)$ .

The present work is primarily theoretical, combining the system-wide heat transfer derivations of natural and forced convections from Jaffer [5] and Jaffer [2], respectively. It applies to convex flat surfaces at any inclination having isotropic roughness with  $0 < \varepsilon \ll L$  and forced flow parallel to the surface.

Table 1 Rowley et al. mixed convection data-sets

Surface	$\theta$	$\psi$	$Ra \geq$	$Ra \leq$	$Re \geq$	$Re \leq$	Count
smooth-plaster	0.0°	90.0°	$2.8 \times 10^6$	$1.1 \times 10^7$	$7.9 \times 10^4$	$8.3 \times 10^4$	2
smooth-plaster	0.0°	90.0°	$3.1 \times 10^6$	$1.1 \times 10^7$	$6.7 \times 10^4$	$7.1 \times 10^4$	2
smooth-plaster	0.0°	90.0°	$3.2 \times 10^6$	$1.1 \times 10^7$	$5.6 \times 10^4$	$5.9 \times 10^4$	2
smooth-plaster	0.0°	90.0°	$3.7 \times 10^6$	$1.1 \times 10^7$	$4.5 \times 10^4$	$4.7 \times 10^4$	2
smooth-plaster	0.0°	90.0°	$4.1 \times 10^6$	$1.2 \times 10^7$	$3.4 \times 10^4$	$3.5 \times 10^4$	2
smooth-plaster	0.0°	90.0°	$5.0 \times 10^6$	$1.2 \times 10^7$	$2.2 \times 10^4$	$2.3 \times 10^4$	2
concrete	0.0°	90.0°	$1.1 \times 10^7$	$1.1 \times 10^7$	$7.9 \times 10^4$	$7.9 \times 10^4$	1
concrete	0.0°	90.0°	$7.9 \times 10^6$	$1.1 \times 10^7$	$6.7 \times 10^4$	$6.9 \times 10^4$	3
concrete	0.0°	90.0°	$2.9 \times 10^6$	$1.1 \times 10^7$	$5.6 \times 10^4$	$5.9 \times 10^4$	7
concrete	0.0°	90.0°	$3.1 \times 10^6$	$1.1 \times 10^7$	$4.5 \times 10^4$	$4.7 \times 10^4$	2
concrete	0.0°	90.0°	$3.9 \times 10^6$	$1.1 \times 10^7$	$3.4 \times 10^4$	$3.5 \times 10^4$	2
concrete	0.0°	90.0°	$4.3 \times 10^6$	$1.2 \times 10^7$	$2.2 \times 10^4$	$2.4 \times 10^4$	2
brick	0.0°	90.0°	$2.0 \times 10^6$	$1.1 \times 10^7$	$6.4 \times 10^4$	$6.7 \times 10^4$	6
brick	0.0°	90.0°	$3.4 \times 10^6$	$1.1 \times 10^7$	$5.5 \times 10^4$	$5.8 \times 10^4$	4
brick	0.0°	90.0°	$2.7 \times 10^6$	$1.1 \times 10^7$	$4.5 \times 10^4$	$4.7 \times 10^4$	3
brick	0.0°	90.0°	$3.1 \times 10^6$	$1.1 \times 10^7$	$4.0 \times 10^4$	$4.2 \times 10^4$	5
brick	0.0°	90.0°	$4.3 \times 10^6$	$1.1 \times 10^7$	$3.0 \times 10^4$	$3.2 \times 10^4$	4
brick	0.0°	90.0°	$5.3 \times 10^6$	$1.1 \times 10^7$	$1.7 \times 10^4$	$1.8 \times 10^4$	4
rough-plaster	0.0°	90.0°	$1.1 \times 10^7$	$1.1 \times 10^7$	$6.7 \times 10^4$	$6.7 \times 10^4$	1
rough-plaster	0.0°	90.0°	$3.6 \times 10^6$	$1.1 \times 10^7$	$5.6 \times 10^4$	$5.9 \times 10^4$	2
rough-plaster	0.0°	90.0°	$3.7 \times 10^6$	$1.1 \times 10^7$	$4.5 \times 10^4$	$4.7 \times 10^4$	2
rough-plaster	0.0°	90.0°	$4.0 \times 10^6$	$1.2 \times 10^7$	$3.4 \times 10^4$	$3.5 \times 10^4$	3
rough-plaster	0.0°	90.0°	$4.8 \times 10^6$	$1.2 \times 10^7$	$2.2 \times 10^4$	$2.4 \times 10^4$	2
stucco	0.0°	90.0°	$1.1 \times 10^6$	$1.1 \times 10^7$	$6.7 \times 10^4$	$7.1 \times 10^4$	2
stucco	0.0°	90.0°	$6.9 \times 10^5$	$1.1 \times 10^7$	$5.6 \times 10^4$	$6.0 \times 10^4$	3
stucco	0.0°	90.0°	$1.2 \times 10^6$	$1.1 \times 10^7$	$4.5 \times 10^4$	$4.8 \times 10^4$	3
stucco	0.0°	90.0°	$1.5 \times 10^6$	$1.1 \times 10^7$	$3.4 \times 10^4$	$3.6 \times 10^4$	3
stucco	0.0°	90.0°	$2.1 \times 10^6$	$1.1 \times 10^7$	$2.2 \times 10^4$	$2.4 \times 10^4$	2

**1.8 Not Empirical.** Empirical theories derive their coefficients from measurements, inheriting the uncertainties from those measurements. Theories developed from first principles derive their coefficients mathematically. For example, Incropera, DeWitt, Bergman, and Lavine [16] (p. 210) gives the thermal conductance of one face of a diameter  $D$  disk into a stationary, uniform medium having thermal conductivity  $k$  as exactly  $8k/[\pi D]$  (units  $\text{W}/(\text{m}^2 \cdot \text{K})$ ). The present theory derives from first principles; it is not empirical. Each formula is tied to aspects of the plate geometry and orientation, fluid, and flow.

**1.9 RMS Relative Error.** Root-mean-squared (RMS) relative error (RMSRE) provides an objective, quantitative evaluation of experimental data versus theory. It gauges the fit of measurements  $g(Re_j)$  to function  $f(Re_j)$ , giving each of the  $n$  samples equal weight in Formula (5). Along with presenting RMSRE, charts in the present work split RMSRE into the bias and scatter components defined in Formula (6). The root-sum-squared of bias and scatter is RMSRE.

$$\text{RMSRE} = \sqrt{\frac{1}{n} \sum_{j=1}^n \left| \frac{g(Re_j)}{f(Re_j)} - 1 \right|^2} \quad (5)$$

$$\text{bias} = \frac{1}{n} \sum_{j=1}^n \left\{ \frac{g(Re_j)}{f(Re_j)} - 1 \right\} \quad \text{scatter} = \sqrt{\frac{1}{n} \sum_{j=1}^n \left| \frac{g(Re_j)}{f(Re_j)} - 1 - \text{bias} \right|^2} \quad (6)$$

## 2. Natural Convection

Jaffer [5] derived a natural convection formula for external flat plates (with convex perimeter) in any orientation from its analyses of horizontal and vertical plates. This investigation uses the same approach.

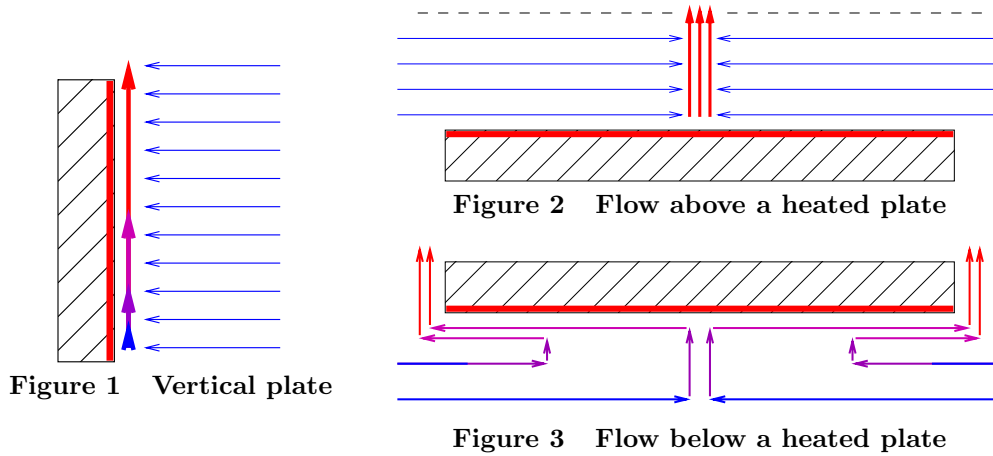
Figures 1, 2, and 3 show the induced fluid flows around heated vertical and horizontal surfaces.

For a horizontal plate with heated upper face, streamlines photographs in Fujii and Imura [3] show natural convection pulling fluid horizontally from above the plate's perimeter into a rising central plume. Figure 2 is a diagram of this upward-facing convection. Horizontal flow is nearly absent at the elevation of the dashed line.

The streamlines photograph of a vertical plate in Fujii and Imura [3] shows fluid being pulled horizontally before rising into a plume along the vertical plate. Figure 1 is its diagram.

Modeled on a streamlines photograph in Aihara, Yamada, and Endö [17], Figure 3 is a flow diagram for a horizontal plate with heated lower face. Unheated fluid below the plate flows horizontally inward. It rises a short distance, flows outward closely below the plate, and flows upward upon reaching the plate edge. The edge flows self-organize so that they are at the opposing edges of the plate which are nearest to each other.

Horizontal flow in Figure 2 is radial, but not radial in Figure 3.



An important aspect of all three flow topologies is that fluid is pulled horizontally before being heated by the plate. Pulling horizontally expends less energy than pulling vertically because the latter does work against the gravitational force. Inadequate horizontal (or vertical) clearance around a plate can obstruct flow and reduce convection and heat transfer; such a plate is not “external”.

From thermodynamic constraints, Jaffer [5] derives generalized natural convection Formula (7) with the parameters specified in Table 2:

- $\theta$  is the angle of the plate from vertical;
- $L$  is the characteristic length of a flat plate with convex perimeter:
  - face up  $L^*$  is the area-to-perimeter ratio;
  - vertical  $L'$  is the harmonic mean of the perimeter vertical spans (the height of a level rectangle);
  - face down  $L_R$  is the harmonic mean of the perimeter distances to that bisector which is perpendicular to the shortest bisector (1/2 of the shorter side of a rectangle);

- $Nu_0$  is the conduction into the fluid when not moving (static);
- $Ra'$  is computed with vertical  $L'$ ;  $Ra^* = Ra' [L^*/L']^3$ ;  $Ra_R = Ra' [L_R/L']^3$ .

$Pr$  does not affect upward-facing heat transfer because the heated fluid flows directly upward, as does conducted heat. When heated fluid must flow along vertical and downward-facing plates, its heat transfer potential is reduced by dividing  $Ra$  by  $\Xi$  from Formula (8).

- $E$  is the count of  $90^\circ$  changes in direction of fluid flow;
- $B$  is the sum of the mean lengths of flows parallel to the plate divided by  $L$ ;
- $C$  is the plate area fraction responsible for flow induced heat transfer;
- $D$  is the effective length of heat transfer contact with the plate divided by  $L$ ;
- The  $\ell^p$ -norm combines the static conduction and induced convective heat flows.

**Table 2** Natural convection parameters

Face	$\theta$	$L$	$\overline{Nu}$	$Nu_0$	$Ra$	$E$	$B$	$C$	$D$	$p$
up	$-90^\circ$	$L^*$	$\overline{Nu}^*$	$Nu_0^*$	$Ra^*$	1	2	$1/\sqrt{8}$	1	$1/2$
vertical	$0^\circ$	$L'$	$\overline{Nu}'$	$Nu_0'$	$Ra'/\Xi$	1	$1/2$	$1/2$	$1/4$	$1/2$
down	$+90^\circ$	$L_R$	$\overline{Nu}_R$	$Nu_0'/2$	$Ra_R/\Xi$	3	4	$1/2$	2	1

$$\overline{Nu} = \left\| Nu_0 [1 - C], {}^{2+E}\sqrt{[C D Nu_0]^{3+E} \frac{2}{B} Ra} \right\|_p \quad (7)$$

$$\Xi = \left\| 1, \frac{0.5}{Pr} \right\|_{\sqrt{1/3}} \quad Nu_0^* = \frac{2}{\pi} \quad Nu_0' = \frac{2^4}{\sqrt[4]{2} \pi^2} \quad (8)$$

**2.1 Effective Vertical Reynolds Number.** From the derivation in Jaffer [5] with  $Ra'/\Xi \gg 1$ ,  $\overline{Nu} \approx C D Nu_0 Re$ . Heat transfer  $\overline{Nu}'$  is reduced by the self-obstruction factor  $1/\sqrt[3]{\Xi}$ , which grows with  $Pr$ . However, heat transfer is not the same as fluid flow, which increases with decreasing  $Pr$ . The  $\Xi^3$  factor in Formula (9) makes  $Re_N$  increase with decreasing  $Pr$ . Proposed is Formula (9) as the Reynolds number associated with the natural convective flow from a vertical plate.

$$Re_N \approx \frac{\overline{Nu} \Xi^{2+E}}{Nu_0 C D} = \frac{8 \overline{Nu}' \Xi^3}{Nu_0'} \quad \overline{Nu}' \gg Nu_0' \quad (9)$$

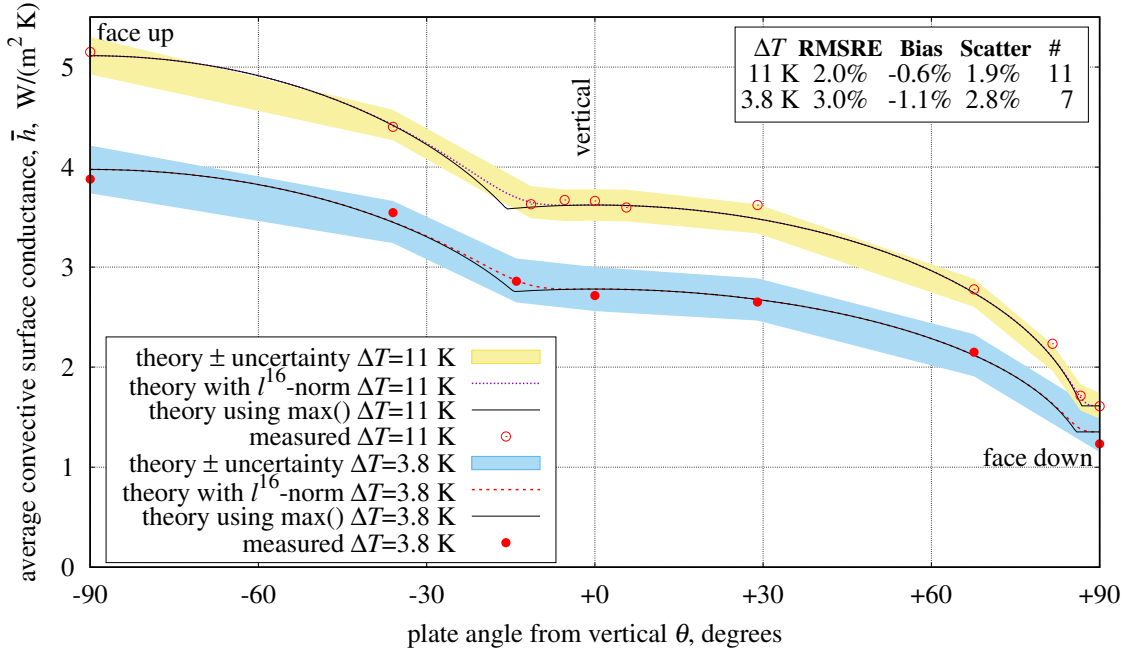


**Figure 4** Natural convection versus angle

**2.2 Natural Convection From an Inclined Plate.**  $Ra$  is proportional to gravitational acceleration. Following the approach of Fujii and Imura [3], the  $Ra$  argument to  $\overline{h}'(Ra) \equiv k \overline{Nu}'(Ra)/L'$  is scaled by  $|\cos \theta|$ , modeling the reduced convection of a tilted plate as a reduction in gravitational acceleration. Similarly, the  $Ra$  arguments to  $\overline{h}^*$  and  $\overline{h}_R$  are scaled by  $|\sin \theta|$ . An unobstructed plate induces a single steady-state mode of natural convection (face up, down, or vertical). The instances of  $\max()$  in Formula (10) choose the largest surface conductance among these modes.

$$\overline{h} = \begin{cases} \max(\overline{h}'(|\cos \theta| Ra'/\Xi), \overline{h}^*(|\sin \theta| Ra^*)) & \sin \theta < 0 \\ \max(\overline{h}'(|\cos \theta| Ra'/\Xi), \overline{h}_R(|\sin \theta| Ra_R/\Xi)) & \sin \theta \geq 0 \end{cases} \quad (10)$$

In reality, the  $\theta$  transition is more gradual using the  $\ell^{16}$ -norm in Formula (11):

$$\bar{h} = \begin{cases} \|\bar{h}'(|\cos \theta| Ra' / \Xi), \bar{h}^*(|\sin \theta| Ra^*)\|_{16} & \sin \theta < 0 \\ \|\bar{h}'(|\cos \theta| Ra' / \Xi), \bar{h}_R(|\sin \theta| Ra_R / \Xi)\|_{16} & \sin \theta \geq 0 \end{cases} \quad (11)$$

**2.3 Rough Natural Convection.** The agreement of rough plate measurements with theory over the  $\pm 90^\circ$  range in Figure 4 indicates that Formula (11) governs plates with RMS height-of-roughness  $0 \leq \varepsilon \ll L$ .

### 3. Forced Convection

Forced convection  $\overline{Nu}$  is the heat transfer caused by forced flow along (and parallel to) a heated plate. The surface conductance  $\bar{h}_F \equiv \overline{Nu} k / L$  grows with  $Re_F$ ,  $Pr$ , and  $k$ . Its characteristic length  $L$  is the length of the plate in the direction of forced flow.

**3.1 Rough Convection.** Jaffer [2] derives the forced convection  $\overline{Nu}_\rho$  of rough flow from isotropic, periodic roughness:

$$\overline{Nu}_\rho(Re_F) = \frac{Re_F Pr_\infty^{1/3} w}{6 [\ln(L/\varepsilon)]^2} \quad Re_F > \left[ \frac{0.664}{\varepsilon} \right]^2 L_P L \quad (12)$$

$$w = \left\| 1, \frac{\varepsilon}{L_W} \right\|_{\sqrt{1/2}} \quad (13)$$

- $\varepsilon \ll L$  is the root-mean-squared (RMS) height of roughness.
- $L_P \ll L$  is the isotropic period of the roughness (Jaffer [2]).
- $L_W$  is the width of the plate (perpendicular to  $L$ ).
- $Pr_\infty$  is the bulk fluid's Prandtl number (far from the plate).

If the roughness extends to the plate's rim, then it increases the effective width of the rough face by more than  $2\varepsilon$  because, in addition to the fluid adjacent to plate's face and rim, the fluid near the edge between them is affected. Thus  $\varepsilon$  and plate width  $L_W$  cooperate weakly, leading to an effective width of  $\|L_W, \varepsilon\|_{\sqrt{1/2}}$ . Dividing by  $L_W$ , Formula (13) is the edge roughness correction factor  $w$ . Figure 5 graphs  $w$  as a function of  $\varepsilon$ .

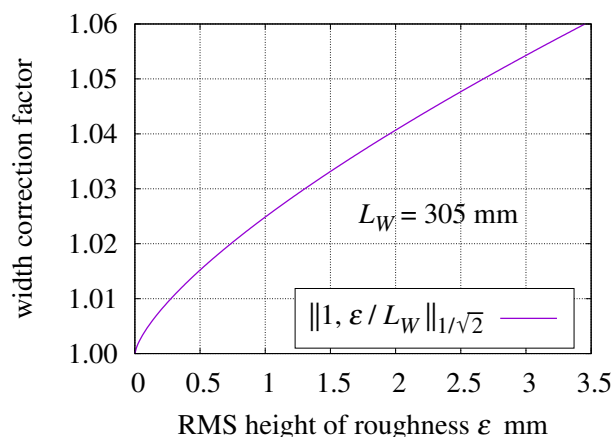


**Figure 5** Edge roughness correction factor

**3.2 Plateau Roughness.** There are isotropic, periodic roughnesses whose convective heat transfer differs from Formula (12).

- Informally, a “plateau roughness” is an isotropic, periodic roughness with most of its area at its peak elevation. A quantitative definition is given in Jaffer [2].
- A “plateau wells roughness” is an array of co-planar wells dropping below a flat surface.
- A “plateau islands roughness” is an array of co-planar islands.

The present apparatus plate has plateau islands roughness.

For a given  $Re_F$ , a plateau roughness may contain areas transferring heat per Formula (12), and separate areas transferring heat as turbulent flow along a smooth plate, but with characteristic length  $L_P$ .

**3.3 Turbulent Forced Convection.** Jaffer [2] derives the average surface conductance,  $\overline{h_F} \equiv \overline{Nu_\tau} k/L$ , of turbulent flow along an isothermal plate as Formula (14).

$$\overline{Nu_\tau} = \frac{Nu_0 Re_F \overline{f_\tau}}{\sqrt{3}} \sqrt{\frac{Pr/\sqrt{162} + 1}{\sqrt{162} Pr \overline{f_\tau} + 1}} \sqrt[3]{\frac{Pr/\Xi}{\|1, 1/Pr\|_3}} \quad \sqrt{162} \equiv 9\sqrt{2} \approx 12.7 \quad (14)$$

$$\overline{f_\tau} = \frac{2^{-5/4}}{[W_0(Re_F/\sqrt{3}) - 1]^2} \quad \Xi = \left\| 1, \frac{0.5}{Pr} \right\|_{\sqrt{1/3}} \quad Nu_0 = \frac{2^4}{\pi^2 \sqrt[4]{2}} \quad (15)$$

- The fluid's effective Prandtl number  $Pr = Pr_W^{1/4} Pr_\infty^{3/4}$  (from Žukauskas and Šlančiauskas [18]).  
 $Pr_W$  is the Prandtl number of fluid at wall (plate) temperature.  
 $Pr_\infty$  is the Prandtl number of fluid at the bulk flow temperature.
- $W_0$  is the principal branch of the Lambert W function, defined as  $W_0(\varphi \exp \varphi) = \varphi$  when  $\varphi \geq 0$ .
- In Formula (15),  $2^{-5/4}$  replaces the  $\sqrt[3]{2}/3$  coefficient from Jaffer [2], a +0.11% correction.
- Plateau islands roughness can shed rough and turbulent flow simultaneously.

#### 3.4 Plateau Islands Roughness.

The plateau islands roughness described in (appendix) Section 16 has  $\overline{Nu_\rho}$  Formula (12) rough convection in the leading  $Re_I/Re_F$  portion of the plate, and  $\overline{Nu_I}$  Formula (16) turbulent convection in the rest of the plate. Formula (17)  $Re_I$  separates the regions, where  $L^\bullet$  is the ratio of each (convex) island's area to its perimeter.

$$\overline{Nu_I} = \left\{ 1 - \Omega + \left\| \frac{\Omega}{2}, \frac{2\varepsilon[4L^\bullet]}{L_P^2} \right\|_2 \right\} \frac{L}{L_P} \overline{Nu_\tau} \left( \frac{Re_F L_P}{L} \right) \quad (16)$$

$$Re_I = \frac{3^3 \varepsilon^2 L^2}{L^\bullet L_P^3} \ln \frac{3^3 \varepsilon^2 L^2}{\sqrt{3} L^\bullet L_P^3} \quad (17)$$

$$\overline{Nu_t} = \overline{Nu_I}(Re_F) + \overline{Nu_\rho}(\|Re_F, Re_I\|_{-4}) - \overline{Nu_I}(\|Re_F, Re_I\|_{-4}) \quad (18)$$

“Openness”  $0 < \Omega < 1$  is the non-plateau area per cell area ratio. Given a  $w \times w$  matrix of elevations  $S_{s,t}$ :

$$\Omega \approx \frac{1}{w^2} \sum_{t=0}^{w-1} \sum_{s=0}^{w-1} \begin{cases} 1, & \text{if } S_{s,t} < \max(S) - \varepsilon^2/L_P; \\ 0, & \text{otherwise.} \end{cases} \quad (19)$$

In the log-log plots in Figures 6 and 7, the effective  $Re_F$  exponent is the slope of its line. For example, the “ $Re_F/200$ ” and “ $Re_F/333$ ” lines have slope 1; thus they are proportional to  $Re_F^1 \equiv Re_F$ . In each plot, the “bi-level” trace is  $\overline{Nu_t}$  Formula (18). The “turbulent part” trace is Formula (20), which is the turbulent component of  $\overline{Nu_t}$  Formula (18):

$$\overline{Nu_I}(Re_F) - \overline{Nu_I}(\|Re_F, Re_I\|_{-4}) \quad (20)$$

In both Figures 6 and 7, the slope of the Formula (20) “turbulent part” trace is close to 1 through more than an order of magnitude of  $Re_F$ . The discrepancy at larger  $Re_F$  is unimportant because the heat transfer is dominated by forced convection in that range.



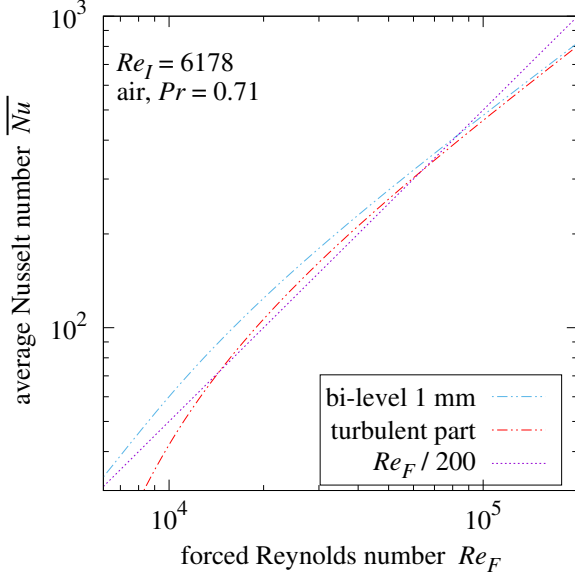


**Figure 6** Forced convection  $Re_I = 6178$

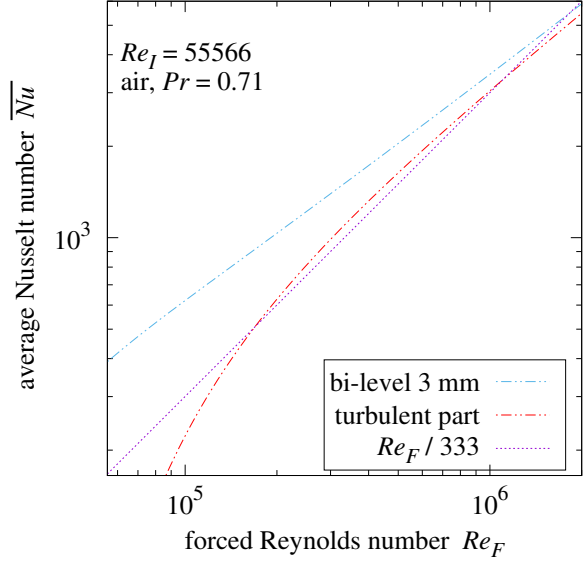


**Figure 7** Forced convection  $Re_I = 55566$

#### 4. Mixing Natural and Forced Convections

The previous sections established that:

- The effective natural Reynolds number  $Re_N$  is proportional to  $\overline{Nu}_N$  when  $\overline{Nu}_N \gg Nu_0$ .
- Forced rough convection  $\overline{Nu}_\rho$  is proportional to  $Re_F$  in Formula (12).
- And forced turbulent Formula (20) is nearly proportional to  $Re_F$  when  $Re_F > Re_I$ .

On that basis, this investigation proposes:

- Surface conductances  $\overline{h}_N$  and  $\overline{h}_F$  both being proportional to Reynolds numbers indicates that they are commensurate; they can be combined using symmetrical functions such as the  $\ell^p$ -norm.

One approach to predicting mixed convection would be to compute  $\overline{Nu}$  from a function of  $Re_F$  and  $Re_N$ . However, choosing a single  $\overline{Nu}$  formula is problematic; while  $Re$  and  $\overline{Nu}$  are nearly proportional in all three cases, their coefficients are very different. Also, rough convection  $\overline{Nu}_\rho$  is strongly dependent on height-of-roughness  $\varepsilon$ , but Section 2 found that natural convection is insensitive to roughness  $\varepsilon \ll L$ .

- This investigation combines a natural surface conductance  $\overline{h}_N$  (specifically  $\overline{h}^*$ ,  $\overline{h}'$ , or  $\overline{h}_R$ ) with the forced surface conductance  $\overline{h}_F$  using the  $\ell^p$ -norm (where  $p$  depends on plate and flow orientations). Surface conductance  $\overline{h}$  is used instead of  $\overline{Nu}$  in order to avoid characteristic-length mismatch between  $\overline{Nu}$  formulas.

This approach departs from prior works (all of which concerned smooth plates), which compute  $\overline{Nu}$  from a ratio of powers of  $Re_F$  and the Grashof number  $Gr = Ra/Pr$ .

**4.1 Theory and Measurements.** Figures which follow plot  $\overline{Nu}$  at  $L = L'$  measurements and theoretical curves versus  $10^3 < Re_F < 10^5$  using logarithmic scales on both axes. Logarithmic scales do not include 0; the following figures plot the natural convection measurement ( $Re_F = 0$ ) at  $Re_F = 10^3$ .

$\theta$  is the angle of the plate from vertical;  $-90^\circ$  is face up;  $+90^\circ$  is face down.

$\psi$  is the angle of the forced flow from the zenith;  $\psi = 90^\circ$  is horizontal flow;  $\psi = 0^\circ$  is upward. In this investigation, forced flow is always parallel to the plate; hence, horizontal plates have  $\psi = 90^\circ$ .

RMSRE is calculated from the measurements between the vertical lines,  $1950 < Re_F < 5 \times 10^4$ .

The  $\varepsilon = 3$  mm plate sheds only rough flow at  $1950 < Re_F < 5 \times 10^4$ ; its graphs are captioned “rough”. The  $\varepsilon = 1.04$  mm plate sheds rough flow at  $Re_F < Re_I = 6178$  and turbulent flow otherwise. Hence it sheds mostly turbulent flow at  $1950 < Re_F < 5 \times 10^4$ ; its graphs are captioned “turbulent”.

## 5. Horizontal Forced Flow

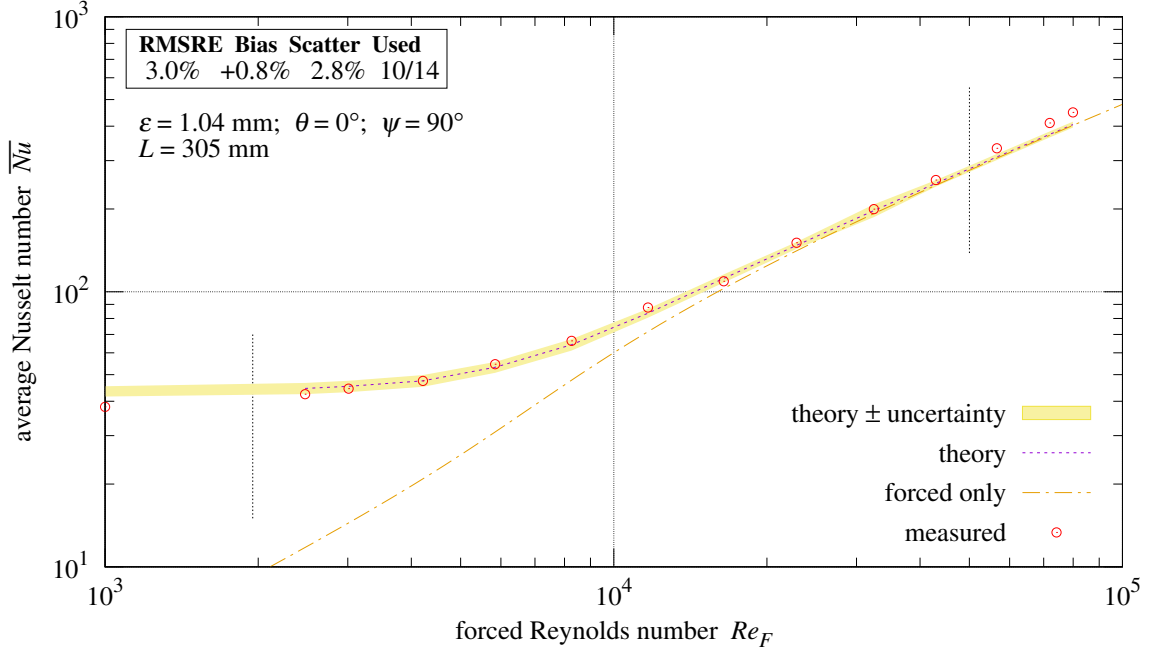


**Figure 8 Vertical plate in horizontal forced turbulent flow**

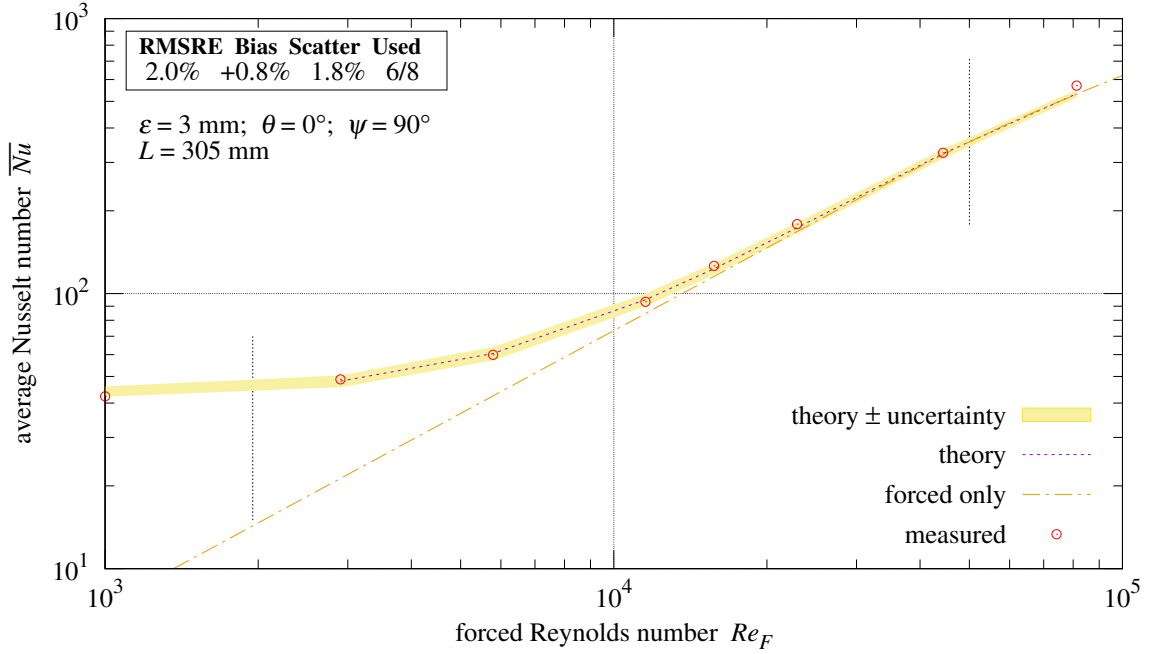


**Figure 9 Vertical plate in horizontal forced rough flow**

**5.1 Vertical Plate With Horizontal Forced Flow.** Figure 1 shows that fluid is drawn horizontally towards the heated surface, then rising. The forced and natural heat flows are thus perpendicular, suggesting the  $\ell^2$ -norm for combining  $\overline{h}_F$  and vertical  $\overline{h}'$ :

$$\overline{h} = \|\overline{h}_F, \overline{h}'\|_2 \quad (21)$$

Figures 8 and 9 compare  $(\overline{Nu} \equiv \overline{h} L/k)$  Formula (21) with measurements of vertical plates in horizontal flow shedding turbulent or rough flow, respectively.

**5.2 American Society of Heating and Ventilation Engineers.** Rowley et al. [15] measured mixed convection of 0.305 m square vertical plates in horizontal flow in a wind tunnel. Their graphs report surface conductance of the plate versus  $T_m$ , the mean of the plate and airflow (Fahrenheit) temperatures. The Rayleigh numbers used by natural convection formulas have the temperature difference as a factor. Through trial and error it was found that taking  $1.05 T_m$  as the (Fahrenheit) plate temperature and  $0.95 T_m$  as the fluid temperature kept RMSRE values less than 10%, which fixed temperature offsets did not. Using coefficients of 1.1 and 0.9 or 1.2 and 0.8 did not strongly affect RMSRE values.

At a constant rate of airflow, increasing fluid temperature causes kinematic viscosity  $\nu$  to grow and  $h_F$  to shrink because  $Re_F = V L/\nu$ . However, the traces in the graphs from Rowley et al. [15] show increasing convective conductance with temperature. Rowley et al. [15] reports the airspeed measured at the center of the duct (of which the rough plate replaces one side). However,  $V$  is defined as the average velocity inside a duct. Let  $V_\odot$  be the velocity at the center of the duct.

The velocity is 0 at the duct wall, so some velocity near the wall must be used as the effective velocity  $V$  at the test plate. The velocity profile across the duct develops from flat at the duct entrance to the Hagen-Poiseuille parabolic velocity profile for a “fully developed” flow (Lienhard and Lienhard [19] p. 356). The dimensionless development length is  $L_D/D = 25.625$ , where  $L_D = 5.207$  m is the duct length between the fan and the leading edge of the plate and  $D = 203.2$  mm is the hydraulic-diameter of the duct.

$V = V_\odot$  when  $L_D = 0$ ; otherwise  $V < V_\odot$ . Dimensional analysis finds that  $V$  must depend on  $V_\odot$ ,  $L_D/D$ ,  $\nu$ , and a viscosity parameter which is independent of temperature. For a gas, let  $\nu_0$  be the viscosity at its boiling point.

Dry air is composed of 78.084% N<sub>2</sub>, 20.946% O<sub>2</sub>, and 0.934% Argon. N<sub>2</sub> has kinematic viscosity  $\nu_0 = 1.15 \times 10^{-6}$  m<sup>2</sup>/s at its 77.355 K boiling point. O<sub>2</sub> has  $\nu_0 = 1.58 \times 10^{-6}$  m<sup>2</sup>/s at its 90.188 K boiling point; Argon gas has  $1.4223 \times 10^{-6}$  m<sup>2</sup>/s at 100 K. Combining these per the air percentages yields  $\overline{\nu_0} = 1.2422 \times 10^{-6}$  m<sup>2</sup>/s. Formula (22) is the effective  $V$  at the plate.

$$V = V_\odot \left/ \left[ 1 + \sqrt{2} \frac{L_D}{D} \frac{\overline{\nu_0}}{\nu} \right] \right. \quad \overline{\nu_0} \approx 1.2422 \times 10^{-6} \frac{\text{m}^2}{\text{s}} \quad (22)$$

**Table 3 Assigned parameters**

Figure	Surface	$\epsilon$	$\varepsilon$
Figure 10	stucco	0.91	1.47 mm
Figure 11	rough-plaster	0.91	0.75 mm
Figure 12	brick	0.93	0.75 mm
Figure 13	concrete	0.94	0.55 mm
Figure 14	smooth-plaster	0.91	0.20 mm

Rowley et al. [15] did not characterize the roughnesses other than to note that the forced convection component was greatest from stucco, followed by brick and rough-plaster, followed by concrete, and the least from smooth-plaster. This investigation has assigned the RMS height-of-roughness ( $\varepsilon$ ) parameters shown in Table 3.

Rowley et al. [15] did not address thermal radiative transfers except to state “In order to obtain average radiation conditions, the inside surface of the test duct was painted a dull gray, and all the pipe outside of the refrigerator was covered with a one-inch thick blanket of insulating material.” Table 3 shows common values for the surface emissivity  $\epsilon$  of each rough material tested. Experimenting with its value, an effective inside surface emissivity of  $\epsilon = 0.70$  keeps all non-stucco RMSRE values less than 5%. Unexpectedly small for paint,  $\epsilon = 0.70$  would compensate for the wind-tunnel walls being warmer than the forced airflow.

Figure 10 shows the mixed convective conductance curves for stucco, the roughest surface Rowley et al. [15] tested. The derivation in Jaffer [2] of rough convection Formula (12) assumes isotropic roughness. Stucco being non-uniform in its application, it has larger RMSRE than the other surfaces.

Figures 11, 12, 13, and 14 compare the present theory with measurements from rough plaster, brick, concrete, and smooth plaster, respectively.<sup>2</sup> Closer to the isotropic ideal, they have RMSRE values smaller than 5%.

<sup>2</sup> One outlying measurement for brick at  $V = 15.65$  m/s was omitted.

Lacking the actual RMS height-of-roughness and emissivities of the original apparatus, while these results lend support to the present theory, they are not conclusive.

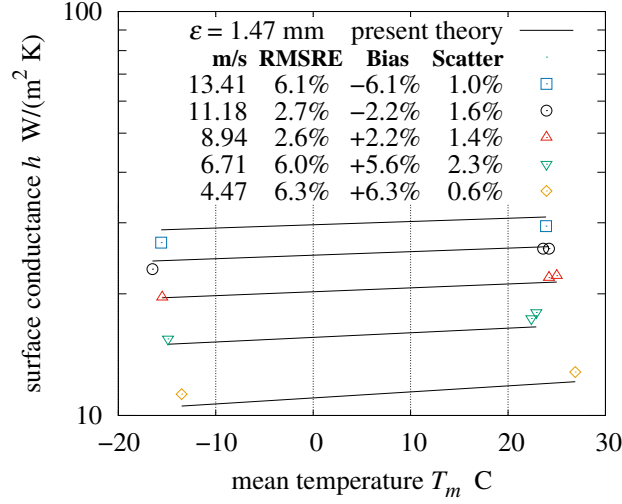


Figure 10 Stucco

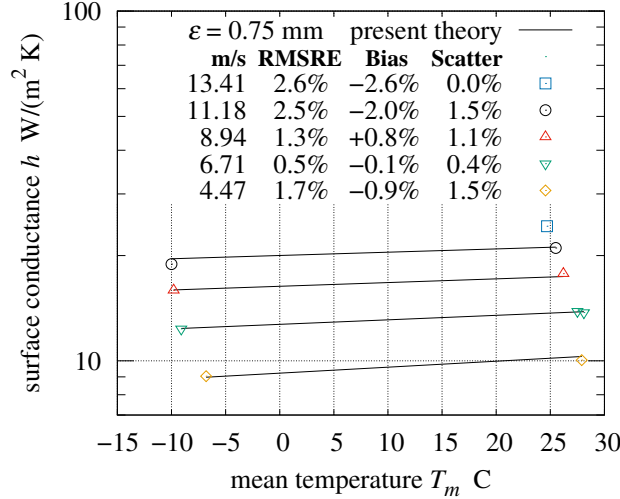


Figure 11 Rough plaster

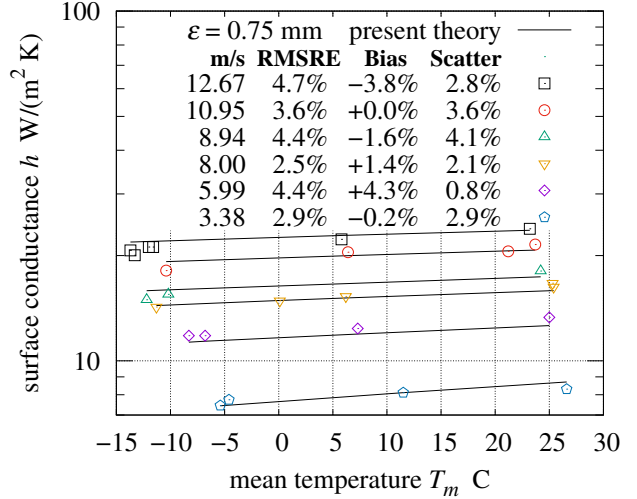


Figure 12 Brick

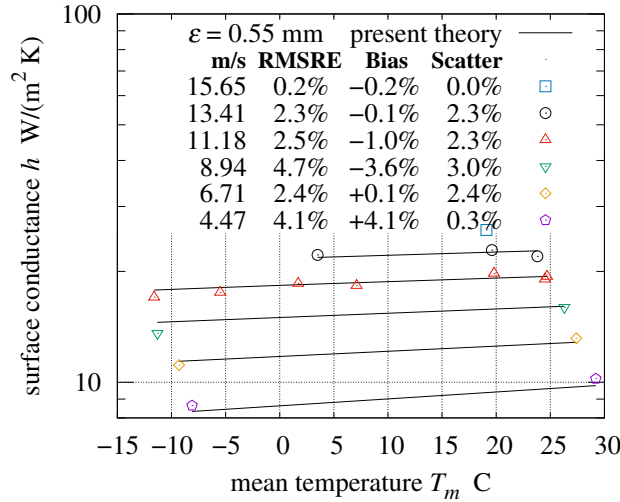


Figure 13 Concrete

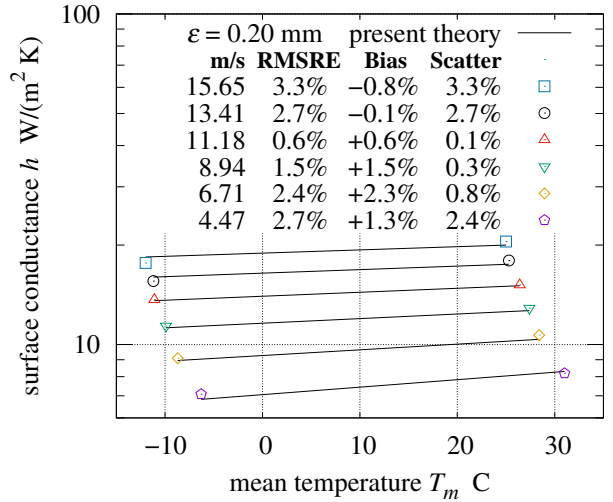


Figure 14 Smooth plaster

**5.3 Upward Facing Plate.** Figure 2 shows that flow is inward above the heated surface. Forced flow parallel to the surface is thus compatible with upward natural convection  $\overline{h}^*$ . Their heat flows are perpendicular, suggesting the  $\ell^2$ -norm for combining  $\overline{h}^*$  and  $\overline{h}_F$ :

$$\overline{h} = \|\overline{h}_F, \overline{h}^*\|_2 \quad (23)$$

Figures 15 and 16 compare Formula (23) with measurements of upward-facing plates shedding turbulent and rough flow, respectively.

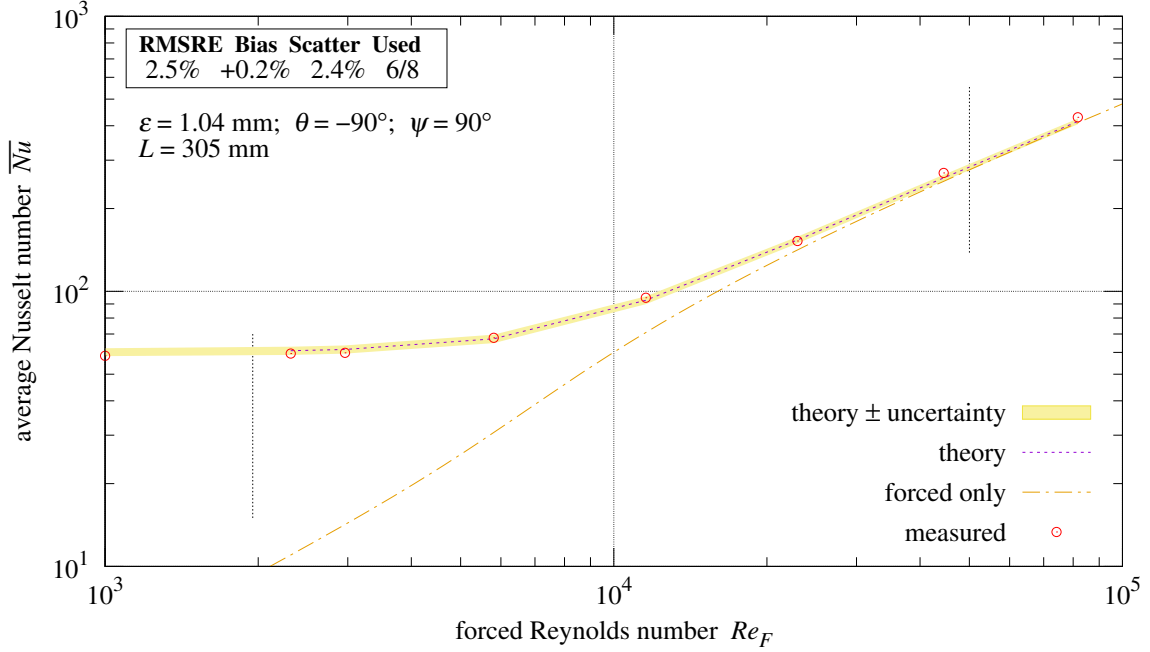


Figure 15 Upward facing plate in horizontal forced turbulent flow

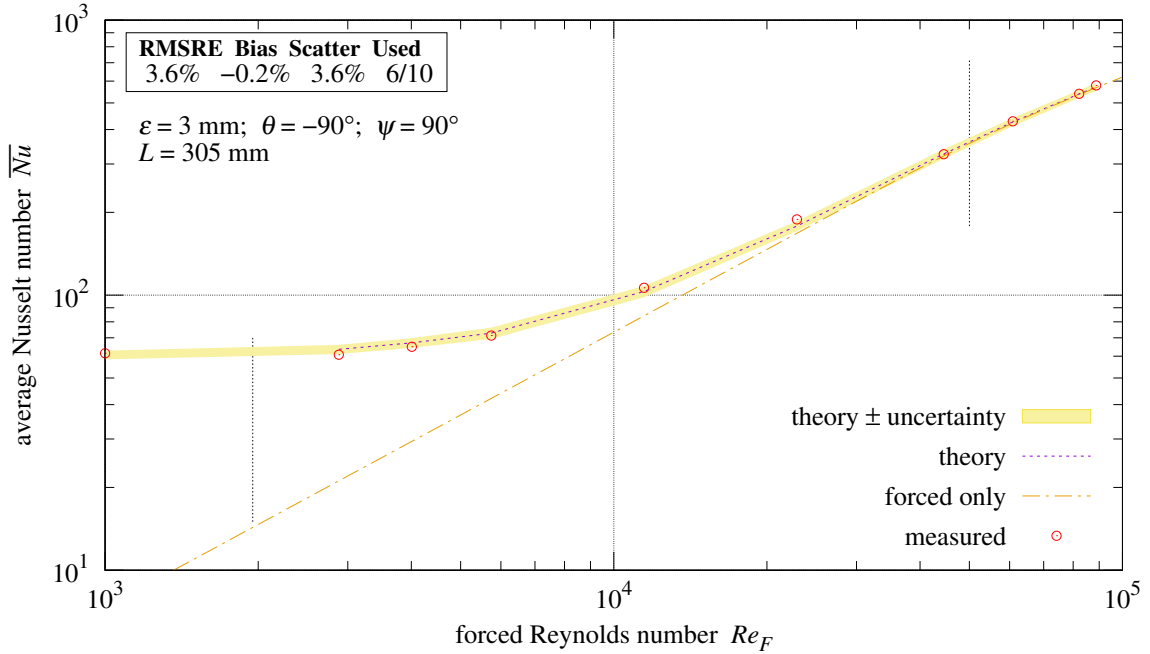
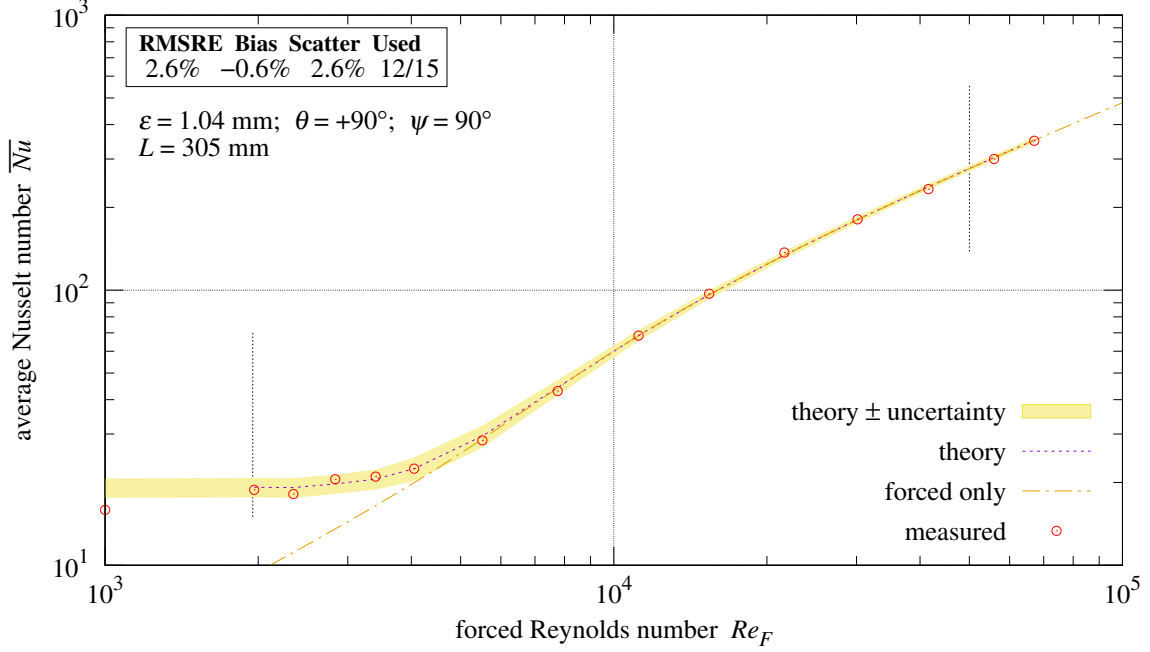


Figure 16 Upward facing plate in horizontal forced rough flow

**5.4 Downward Facing Plate.** Figure 3 shows that flow is outward immediately beneath the heated surface. Forced flow parallel to this surface is thus incompatible with downward natural convection  $\overline{h_R}$ . These two fluid flows will compete for surface area. Table 2 shows that  $\overline{Nu_R}$  is asymptotically proportional to  $\sqrt[5]{Ra_R}$ . The  $\ell^5$ -norm combines  $Ra_R$  with  $Re_F^5$ , manifesting the fragility of  $\overline{h_R}$  flow because moderate  $Re_F$  values can overpower the  $\overline{h_R}$  term:

$$\overline{h} = \|\overline{h_F}, \overline{h_R}\|_5 \quad (24)$$

Figures 17 and 18 compare Formula (24) with measurements of downward-facing plates shedding turbulent or rough flow, respectively.



**Figure 17** Downward facing plate in horizontal forced turbulent flow

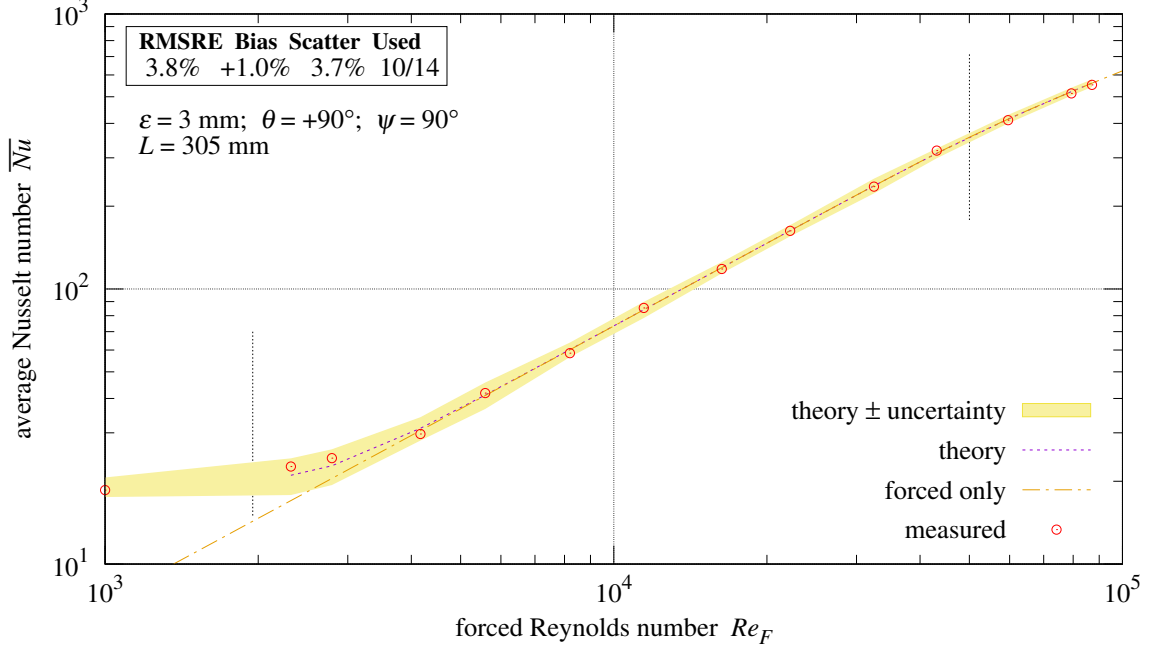


**Figure 18** Downward facing plate in horizontal forced rough flow

## 6. Vertical Plate With Vertical Forced Flow

A vertical plate with vertical forced flow requires a more thorough analysis.

**6.1 Velocity Profiles.** The profile function  $u(y)$  is the velocity at  $x = L/2$  and distance  $0 < y < \delta$  from the plate, where  $\delta$  is the boundary layer thickness at  $x = L/2$ . Positive  $u(y)$  is in the direction of forced flow. The upper plot in Figure 19 shows the profiles of forced turbulent and natural convection adjacent to a vertical 30.5 cm square plate per (appendix) Section 14, as well as their sum and difference profiles.

The widest  $y$  span of constant  $u(y)$  occurs in opposing vertical flows when  $Re_F = Re_N$ . Because of the laminar sublayer of turbulent flows, this cancellation occurs around  $u = 0.065$  m/s, not  $u = 0$ .

The lower plot in Figure 19 shows the theoretical velocity profiles of forced turbulent flow, and that flow combined with laminar natural flow. The forced  $Re_F$  values are double and half of natural  $Re_N$ .

In the opposing flow cases, the “forced – natural” and “forced – natural 21600” traces both have two inflection points near the plate. These indicate that the boundary layer is split, with laminar flow at  $0 < y < 5$  mm and turbulent flow at  $5 < y < 15$  mm.

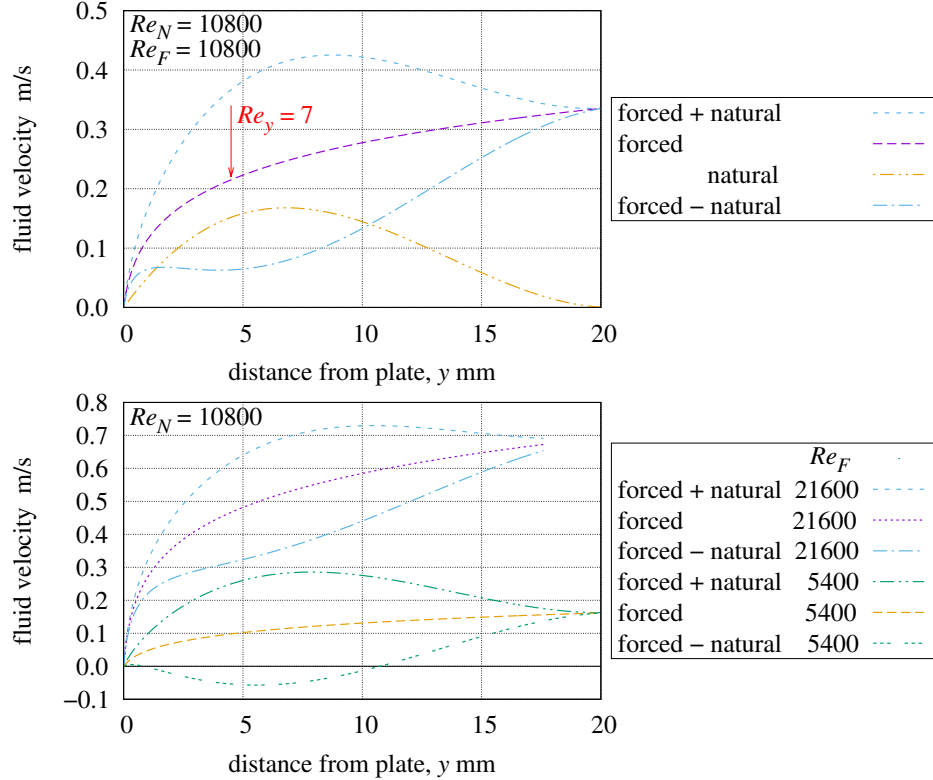


Figure 19 Velocity profiles

**6.2 Vertical Plate With Forced Downward Flow.** Because the net velocity of the “forced – natural 5400” curve goes negative near the plate, these opposing fluid flows compete for plate area.  $\overline{Nu'}$  is asymptotically proportional to  $\sqrt[3]{Ra'}$  in Table 2; the  $\ell^3$ -norm combines  $Ra'$  with  $Re_F^3$  (which is more robust than the  $\ell^5$ -norm):

$$\overline{h} = \|\overline{h_F}, \overline{h'}\|_3 \quad (25)$$

The “forced – natural 21600” trace indicates that its boundary layer is split with laminar natural flow near the plate and forced turbulent flow away. This serves to increase heat transport through the boundary layer (compared with pure laminar), exceeding the  $\ell^2$ -norm, but less than the  $\ell^{\sqrt{2}}$ -norm. The “mixed  $\ell^{\sqrt{3}}$ -norm” curve, Formula (26), is close to the upper measurements in Figures 20 and 21.

$$\overline{h} = \|\overline{h_F}, \overline{h'}\|_{\sqrt{3}} \quad (26)$$

Both the 1 mm and 3 mm plates had plateau islands roughness, as described in Section 3. The  $Re_I$  arrow marks the transition from rough to turbulent flow along the plateau islands roughness.

The  $Re_N$  arrow indicates the position of natural convection's effective Reynolds number calculated by Formula (9). “ $Re_N \chi_I$ ” is  $Re_N$  scaled by the roughness correction ( $\chi_I \geq 1$ ) detailed in (appendix) Section 15; it marks the  $Re_F$  lower-bound of the transition between  $p = 3$  and  $p = \sqrt{3}$ .

When the whole plate is shedding turbulent flow,  $\chi_I = 1$ . When the whole plate is shedding rough flow,  $\chi_I = \chi$ , which is derived in (appendix) Section 14. The close spacing between the arrows in Figure 20 indicates that nearly all of the plate is shedding turbulent flow.

Figures 20 and 21 show the theory curve and the measurements switching from the “mixed  $\ell^3$ -norm” to the “mixed  $\ell^{\sqrt{3}}$ -norm” at  $Re_F > Re_N \chi_I$ .

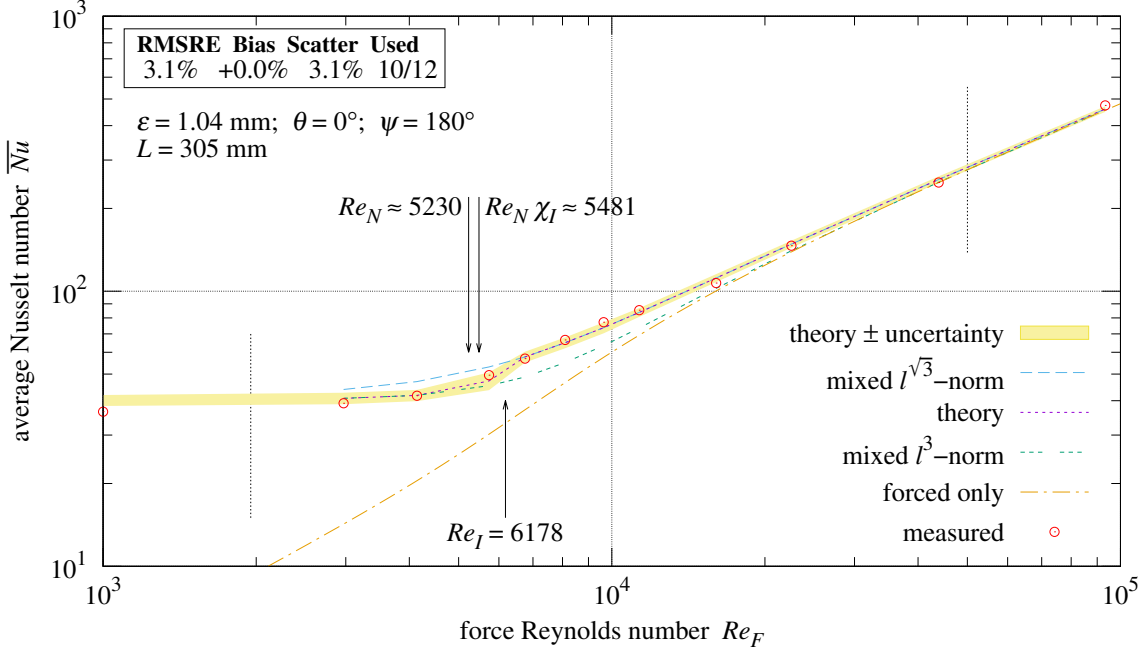


Figure 20 Vertical plate in opposing forced turbulent flow

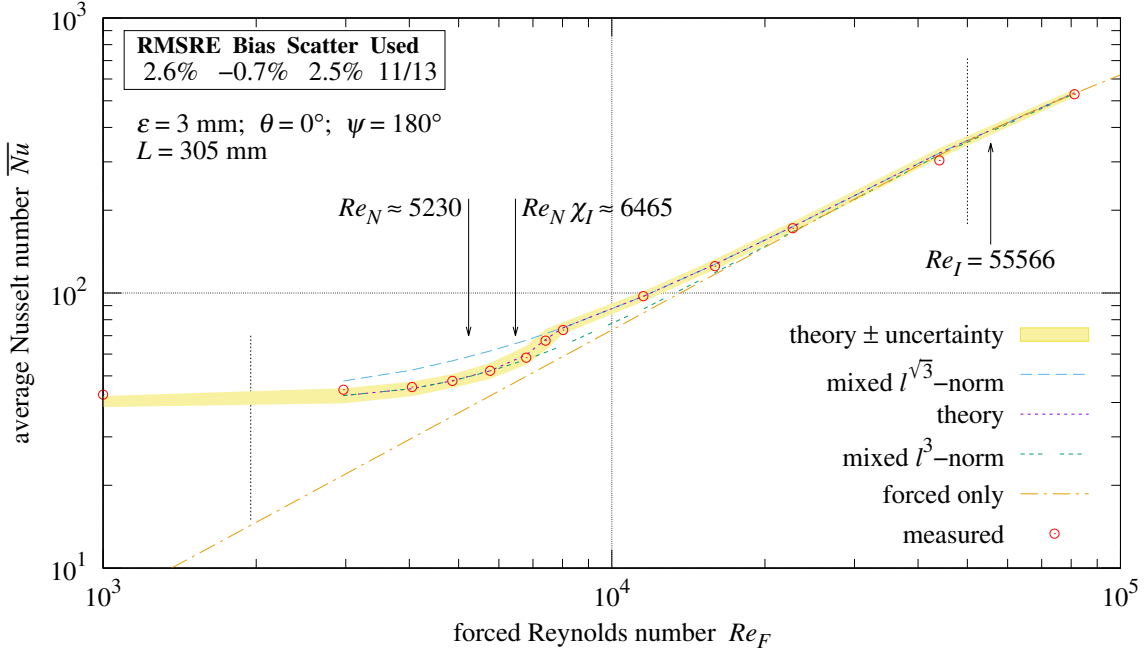


Figure 21 Vertical plate in opposing forced rough flow



**6.3 Vertical Plate With Forced Upward Flow.** At low speeds, the wide separation between the “forced + natural 5400” and “forced 5400” traces in Figure 19 indicates the boundary layer is split, with laminar natural flow near the plate and forced turbulent flow away, leading to  $\bar{h} = \|\bar{h}_F, \bar{h}'\|_{\sqrt{3}}$ .

The steep slope of the “forced + natural 21600” and “forced 21600” traces near the plate indicates that both flows are close to the plate, competing for plate area and leading to  $\bar{h} = \|\bar{h}_F, \bar{h}'\|_3$ .

Figures 22 and 23 show the theory curve and the measurements switching from the “mixed  $\ell^3$ -norm” to the “mixed  $\ell^{\sqrt{3}}$ -norm” at  $Re_F$  smaller than  $Re_N \chi_I$ .

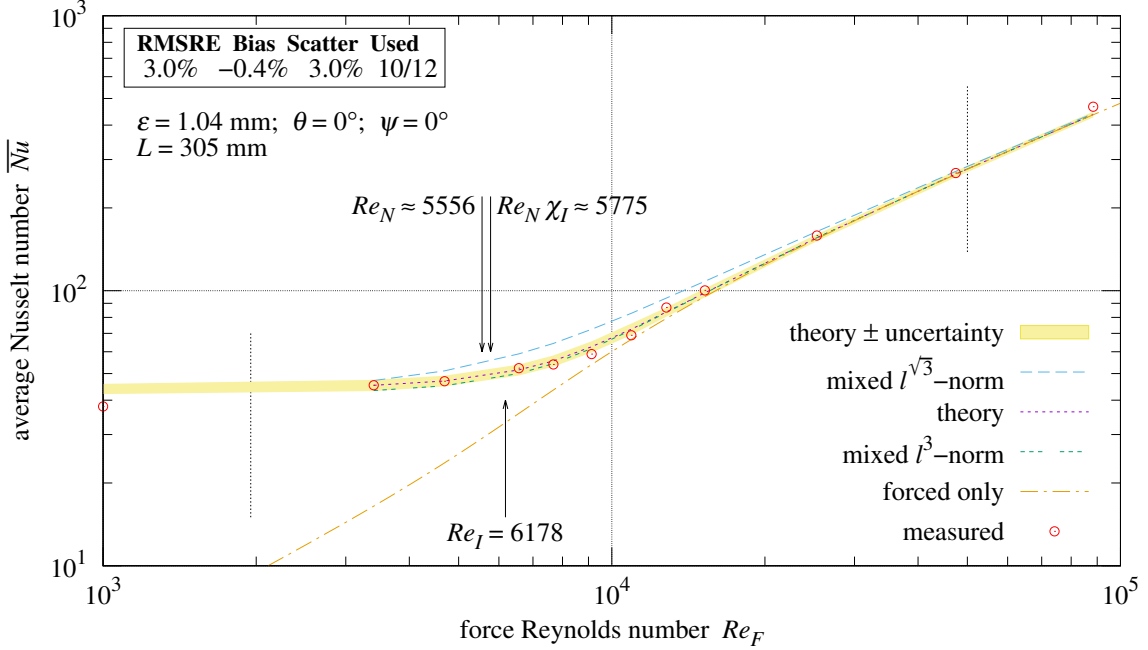


Figure 22 Vertical plate in aiding forced turbulent flow

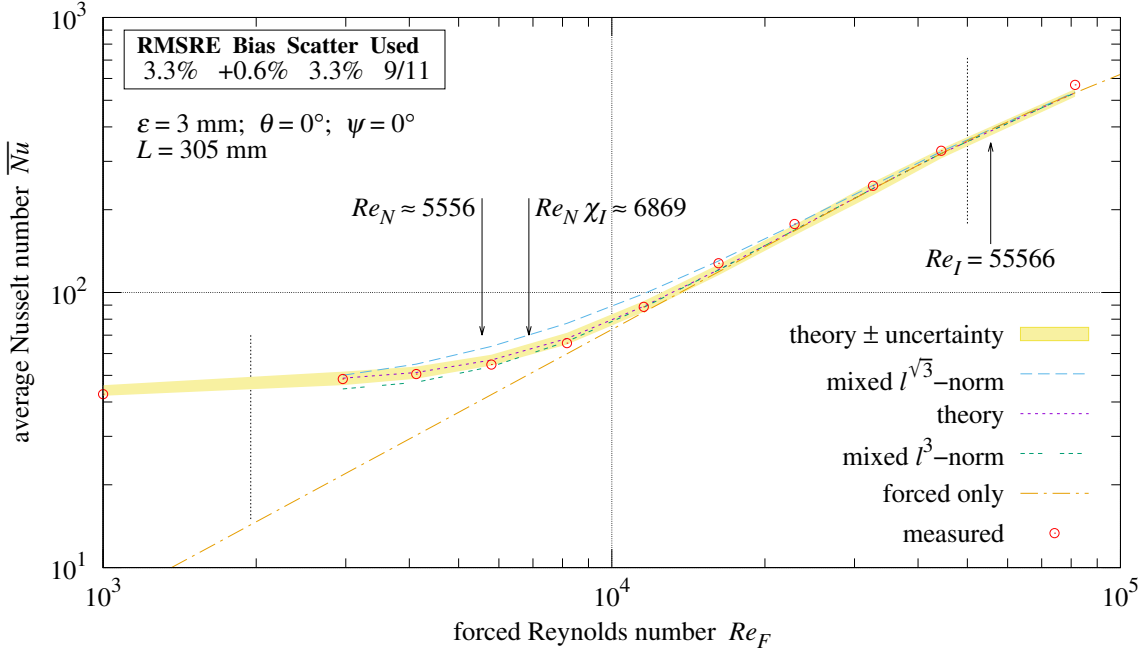


Figure 23 Vertical plate in aiding forced rough flow

## 7. Vertical Plate With Forced Flows at any Angle

All vertical cases examined so far combine  $\overline{h'}$  and  $\overline{h_F}$  using the  $\ell^p$ -norm with  $\sqrt{3} \leq p \leq 3$ . However,  $p$  is a function of  $Re_F$  in the vertical aiding and opposing cases. Needed is a function of  $Re_F$  which varies smoothly between asymptotes  $\sqrt{3}$  and 3. This suggests raising 3 to an exponent between 1/2 and 1. With  $\zeta > 1$  and  $\eta > 0$ , the expression  $\eta^\zeta/\zeta$  varies between 0 and  $\infty$ , and  $\exp_\zeta(-\eta^\zeta/\zeta)$  varies between 0 and 1. Formula (27) varies between  $p = 3$  and  $p = \sqrt{3}$ , with the transition slope controlled by  $\zeta$ .

The aiding flow transition is gradual with  $\zeta = 2$  and  $\eta = Re_N \chi_I / Re_F$ . The opposing flow transition is abrupt with  $\zeta = 16$  and  $\eta = Re_F / [Re_N \chi_I]$ . Note that  $\eta = Re_N \chi_I / Re_F$  differs from  $\eta = Re_F / [Re_N \chi_I]$ .

$$p(\zeta, \eta) = \exp_3(1/2 + \exp_\zeta(-\eta^\zeta/\zeta)/2) \quad (27)$$

Introduced in Section 4,  $\psi$  is the angle between the forced flow and the zenith. Figures 24 and 25 plot  $p$  at  $\zeta = 2$  and  $\zeta = 16$ , used with  $\cos \psi > 0$  and  $\cos \psi < 0$ , respectively. Table 4 lists  $p$  for horizontal and vertical plate and flows.

The theory curve and error statistics in Figures 20, 21, 22, and 23 employ  $p$  Formula (27).

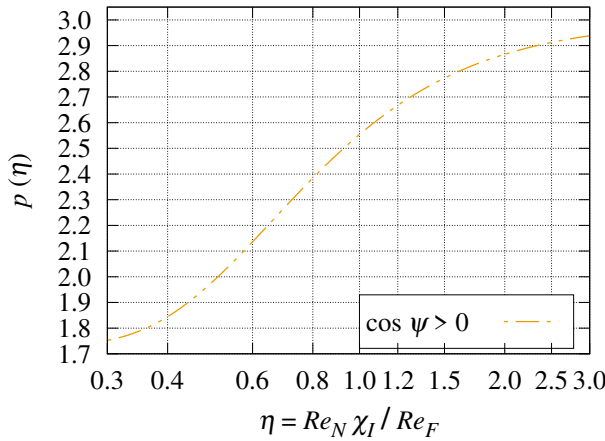


Figure 24 Vertical aiding plate  $p$

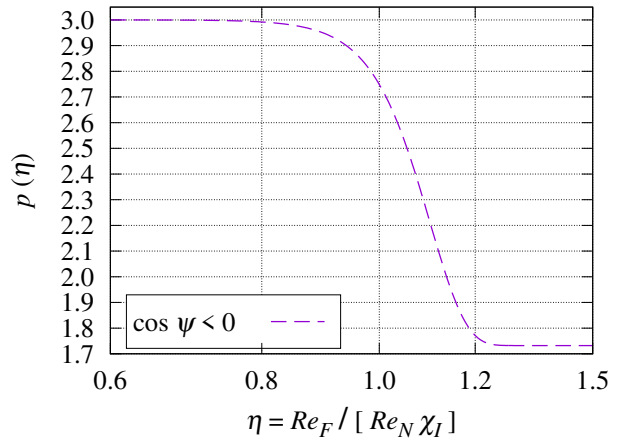


Figure 25 Vertical opposing plate  $p$

Table 4 Corner cases  $p$

Description	$\theta$	$\psi$	$p$
upward facing plate	$-90^\circ$	$90^\circ$	2
aiding vertical plate	$+0^\circ$	$0^\circ$	$\exp_3(1/2 + \exp_2(-[Re_N \chi_I / Re_F]^2/2)/2)$
vertical plate, level flow	$+0^\circ$	$90^\circ$	2
opposing vertical plate	$+0^\circ$	$180^\circ$	$\exp_3(1/2 + \exp_{16}(-[Re_F / [Re_N \chi_I]]^{16}/16)/2)$
downward facing plate	$+90^\circ$	$90^\circ$	5

At  $\psi = 0^\circ$ , the forced and natural flows align. As  $\psi$  tilts toward horizontal ( $\pm 90^\circ$ ), the forced flow can be split into components aligned and perpendicular to the natural upward flow. The coefficients of these components are trigonometric functions of  $\psi$ . Tilting to the left or right of  $\psi = 0^\circ$  by equal angles must transfer the same amount of heat. Thus, the trigonometric coefficients must be “even” functions of  $\psi$ , that is,  $F(\psi) = F(-\psi)$ . Formula (28) coefficients  $[\sin \psi]^2$ ,  $[\cos \psi]^2$ ,  $[\sin \psi]^4$ , and  $[\cos \psi]^4$  are even functions of  $\psi$ .

Downward tilted flow requires a steeper transition slope around  $\psi = 180^\circ$ ; this is implemented using  $[\sin \psi]^4$  and  $[\cos \psi]^4$  as the coefficients in the second line of Formula (28).

$$\overline{h_\theta} = \begin{cases} [\sin \psi]^2 \left\| \overline{h_F}, \overline{h'_\theta} \right\|_2 + [\cos \psi]^2 \left\| \overline{h_F}, \overline{h'_\theta} \right\|_{p(2, Re_N \chi_I / Re_F)} & \text{if } 0 \leq \cos \psi; \\ [\sin \psi]^4 \left\| \overline{h_F}, \overline{h'_\theta} \right\|_2 + [\cos \psi]^4 \left\| \overline{h_F}, \overline{h'_\theta} \right\|_{p(16, Re_F / [Re_N \chi_I])} & \text{if } \cos \psi \leq 0. \end{cases} \quad (28)$$

The vertical natural convection component is independent of  $\psi$ :

$$\overline{h'_\theta} = \overline{h'}(|\cos \theta| Ra' / \Xi) \quad (29)$$

## 8. Mixed Convection From an Inclined Plate

To compute mixed convection from an inclined plate, Formula (30) replaces conductance functions  $\overline{h'}$ ,  $\overline{h^*}$ , and  $\overline{h_R}$  in Formula (11) with  $\ell^p$ -norms mixing each function with  $\overline{h_F}$ .

$$\overline{h} = \begin{cases} \|\overline{h_\theta}, \|\overline{h_F}, \overline{h^*}(\|\sin \theta\| Ra^*)\|_2\|_{16} & 0 \leq \sin \theta \\ \|\overline{h_\theta}, \|\overline{h_F}, \overline{h_R}(\|\sin \theta\| Ra_R/\Xi)\|_5\|_{16} & \sin \theta \leq 0 \end{cases} \quad (30)$$

Figure 26 shows forced flow opposing natural convection at  $\theta = +82^\circ$  with  $\psi = 98^\circ$ . Figure 27 shows forced flow aiding natural convection at  $\theta = \psi = +82^\circ$ . The  $\theta = \psi = +90^\circ$  curve is shown for comparison.

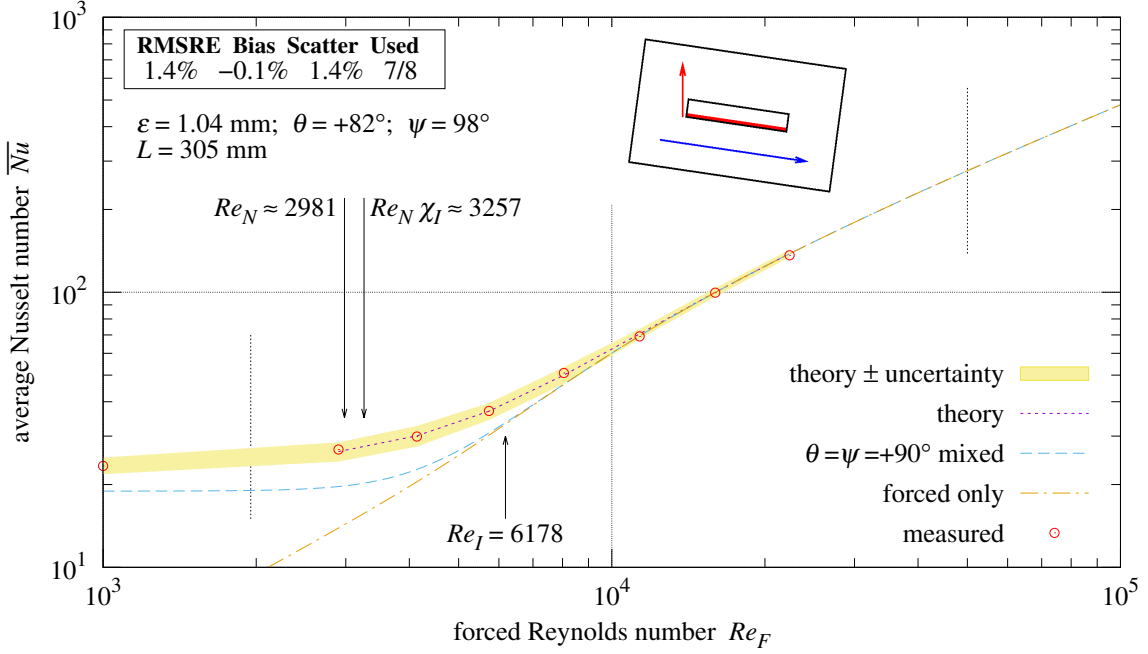


Figure 26 Inclined plate,  $\theta = +82^\circ$ , opposing forced turbulent flow

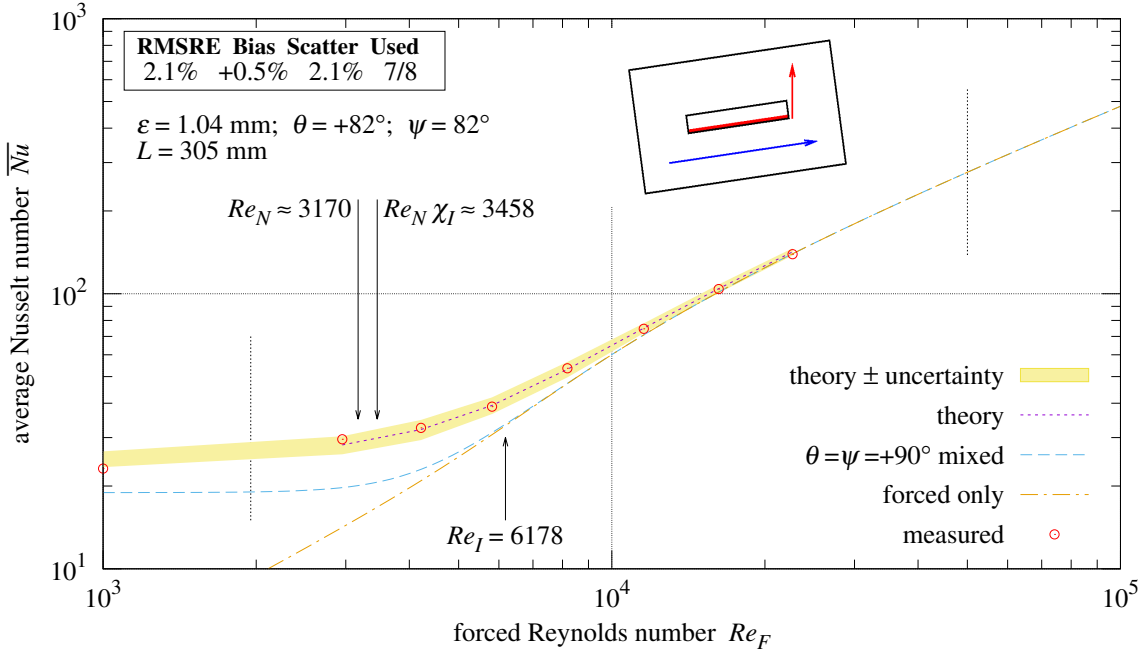


Figure 27 Inclined plate,  $\theta = +82^\circ$ , aiding forced turbulent flow

With  $\overline{h_F} = 0$ , mixed Formula (30) simplifies to natural Formula (11).

When  $\theta$  and  $\psi$  are multiples of  $90^\circ$ , Formula (30) simplifies to  $\|\overline{h_F}, \overline{h_N}\|_p$ , with  $p$  from Table 4.

## 9. Practice

The natural convection heat transfer formulas for  $\overline{h^*}$ ,  $\overline{h'}$ , and  $\overline{h_R}$  were presented in Section 2. The formulas for forced convection heat transfer  $\overline{h_F}$  were presented in Section 3. These are combined using the  $\ell^p$ -norm:

$$\|F_1, F_2\|_p \equiv [|F_1|^p + |F_2|^p]^{1/p} \quad (31)$$

$\theta$  is the angle of the plate from vertical;  $-90^\circ$  is face up;  $+90^\circ$  is face down. Coefficient  $|\sin \theta|$  scales  $Ra^*$  and  $Ra_R$  to model the effect of the plate's inclination as a reduction in the gravitational acceleration.

$$\overline{h} = \begin{cases} \|\overline{h_\theta}, \|\overline{h_F}, \overline{h^*}(|\sin \theta| Ra^*)\|_2\|_{16} & 0 \leq \sin \theta \\ \|\overline{h_\theta}, \|\overline{h_F}, \overline{h_R}(|\sin \theta| Ra_R/\Xi)\|_5\|_{16} & \sin \theta \leq 0 \end{cases} \quad (32)$$

$\psi$  is the angle of the forced flow from the zenith;  $\psi = 0^\circ$  is upward flow;  $\psi = 90^\circ$  is horizontal flow;  $\psi = 180^\circ$  is downward flow. The forced flow is always parallel to the plate.

$$\overline{h_\theta} = \begin{cases} [\sin \psi]^2 \|\overline{h_F}, \overline{h'_\theta}\|_2 + [\cos \psi]^2 \|\overline{h_F}, \overline{h'_\theta}\|_{p(2, Re_N \chi_I / Re_F)} & \text{if } 0 \leq \cos \psi; \\ [\sin \psi]^4 \|\overline{h_F}, \overline{h'_\theta}\|_2 + [\cos \psi]^4 \|\overline{h_F}, \overline{h'_\theta}\|_{p(16, Re_F / [Re_N \chi_I])} & \text{if } \cos \psi \leq 0. \end{cases} \quad (33)$$

The vertical natural convection component  $\overline{h'_\theta}$  is independent of  $\psi$ :

$$\overline{h'_\theta} = \overline{h'}(|\cos \theta| Ra' / \Xi) \quad (34)$$

However, its combination with  $\overline{h_F}$  depends on function  $p(\zeta, \eta)$ , specifically  $p(2, Re_N \chi_I / Re_F)$  when  $\cos \psi \geq 0$ , and  $p(16, Re_F / [Re_N \chi_I])$  when  $\cos \psi \leq 0$ :

$$p(\zeta, \eta) = \exp_3(1/2 + \exp_\zeta(-\eta^\zeta / \zeta) / 2) \quad \exp_b(\varphi) \equiv b^\varphi \quad (35)$$

The  $\chi_I$  factor models the longer path which forced flow takes along plateau islands roughness. The  $\chi$  factor models the longer path which forced flow takes along non-plateau roughness.  $Re_I$  Formula (17) is in Section 3. Use  $Re_I = +\infty$  (which implies  $\chi_I = \chi$ ) for non-plateau roughness.

$$\chi = 1 - 3\sqrt{3} \frac{\varepsilon}{L} \ln \frac{\varepsilon}{L} \quad \chi_I = \exp_\chi\left(\exp_4\left(-[Re_F / Re_I]^4\right)\right) \quad (36)$$

$Re_N$  is the effective Reynolds number of vertical natural convection:

$$Re_N \approx \frac{8 \overline{Nu'} \Xi^3}{Nu'_0} \quad \Xi \equiv \left\| 1, \frac{0.5}{Pr} \right\|_{\sqrt{1/3}} \quad \overline{Nu'} \equiv \frac{\overline{h'} L}{k} \quad Nu'_0 \equiv \frac{2^4}{\sqrt[4]{2} \pi^2} \quad (37)$$

## 10. Results

Table 5 shows the combinations of flow types and orthogonal orientations.

Configurations measured by the present apparatus with its 0.305 m square plates are marked with  $\bullet$ .

Configurations having turbulent natural convection are marked with  $\circ$ . These would require either a larger plate and wind-tunnel or higher plate temperatures than the present apparatus supports.

**Table 5 Mixed convective modes**

Natural	Forced	Vertical	Up	Down	Opposing	Aiding
laminar	turbulent	$\bullet$ Figure 8	$\bullet$ Figure 15	$\bullet$ Figure 17	$\bullet$ Figure 20	$\bullet$ Figure 22
laminar	rough	$\bullet$ Figure 9	$\bullet$ Figure 16	$\bullet$ Figure 18	$\bullet$ Figure 21	$\bullet$ Figure 23
turbulent	turbulent	$\circ$	$\circ$	$\circ$	$\circ$	$\circ$
turbulent	rough	$\circ$	$\circ$	$\circ$	$\circ$	$\circ$

Tables 6 and 7 summarize the present theory’s conformance with 104 measurements in twelve data-sets from the present apparatus’s two plates.

The “ $\varepsilon$ ” column identifies the 30.5 cm square plate used. The 3.00 mm plate had rough flow over the  $1950 < Re_F < 5 \times 10^4$  range. The 1.04 mm plate had turbulent flow over nearly all of the same range. The “Used” column is the count of measurements having  $1950 < Re_F < 5 \times 10^4$  out of the count of measurements. Measurements at  $Re_F > 5 \times 10^4$  were practically unaffected by mixing.

The  $\varepsilon = 3.00$  mm data-sets have RMSRE values between 2.0% and 3.8%.

The  $\varepsilon = 1.04$  mm data-sets have RMSRE values between 1.3% and 3.1%.

**Table 6 Convection measurements versus present theory, forced rough flow**

Description	$\varepsilon$	$\theta$	$\psi$	RMSRE	Bias	Scatter	Used
downward facing plate	3.00 mm	+90.0°	90.0°	3.8%	+1.0%	3.7%	10/14
upward facing plate	3.00 mm	−90.0°	90.0°	3.6%	−0.2%	3.6%	6/10
vertical plate, level flow	3.00 mm	+0.0°	90.0°	2.0%	+0.8%	1.8%	6/8
opposing vertical plate	3.00 mm	+0.0°	180.0°	2.6%	−0.7%	2.5%	11/13
aiding vertical plate	3.00 mm	+0.0°	0.0°	3.3%	+0.6%	3.3%	9/11

**Table 7 Convection measurements versus present theory, forced turbulent flow**

Description	$\varepsilon$	$\theta$	$\psi$	RMSRE	Bias	Scatter	Used
downward facing plate	1.04 mm	+90.0°	90.0°	2.6%	−0.6%	2.6%	12/15
upward facing plate	1.04 mm	−90.0°	90.0°	2.5%	+0.2%	2.4%	6/8
vertical plate, level flow	1.04 mm	+0.0°	90.0°	3.0%	+0.8%	2.8%	10/14
opposing vertical plate	1.04 mm	+0.0°	180.0°	3.1%	+0.0%	3.1%	10/12
aiding vertical plate	1.04 mm	+0.0°	0.0°	3.0%	−0.4%	3.0%	10/12
opposing inclined plate	1.04 mm	+82.0°	98.0°	1.4%	−0.1%	1.4%	7/8
aiding inclined plate	1.04 mm	+82.0°	82.0°	2.1%	+0.5%	2.1%	7/8

Table 8 summarizes the present theory’s conformance with 78 measurements in 28 data-sets on five vertical rough surfaces in horizontal flow from Rowley et al. [15]. The five stucco data-sets have RMSRE values between 2.5% and 6.5%; the other data-sets have RMSRE values between 0.2% and 5%.

Table 8 Rowley et al. mixed convection measurements

Surface	$\epsilon$	$\varepsilon$	$V$	RMSRE	Bias	Scatter	Count
smooth-plaster	0.91	0.20 mm	15.65 m/s	3.3%	-0.8%	3.3%	2
smooth-plaster	0.91	0.20 mm	13.41 m/s	2.7%	-0.1%	2.7%	2
smooth-plaster	0.91	0.20 mm	11.18 m/s	0.6%	+0.6%	0.1%	2
smooth-plaster	0.91	0.20 mm	8.94 m/s	1.5%	+1.5%	0.3%	2
smooth-plaster	0.91	0.20 mm	6.71 m/s	2.4%	+2.3%	0.8%	2
smooth-plaster	0.91	0.20 mm	4.47 m/s	2.7%	+1.3%	2.4%	2
concrete	0.94	0.55 mm	15.65 m/s	0.2%	-0.2%	0.0%	1
concrete	0.94	0.55 mm	13.41 m/s	2.3%	-0.1%	2.3%	3
concrete	0.94	0.55 mm	11.18 m/s	2.5%	-1.0%	2.3%	7
concrete	0.94	0.55 mm	8.94 m/s	4.7%	-3.6%	3.0%	2
concrete	0.94	0.55 mm	6.71 m/s	2.4%	+0.1%	2.4%	2
concrete	0.94	0.55 mm	4.47 m/s	4.1%	+4.1%	0.3%	2
brick	0.93	0.75 mm	12.67 m/s	4.7%	-3.8%	2.8%	6
brick	0.93	0.75 mm	10.95 m/s	3.6%	+0.0%	3.6%	4
brick	0.93	0.75 mm	8.94 m/s	4.4%	-1.6%	4.1%	3
brick	0.93	0.75 mm	8.00 m/s	2.5%	+1.4%	2.1%	5
brick	0.93	0.75 mm	5.99 m/s	4.4%	+4.3%	0.8%	4
brick	0.93	0.75 mm	3.38 m/s	2.9%	-0.2%	2.9%	4
rough-plaster	0.91	0.75 mm	13.41 m/s	2.6%	-2.6%	0.0%	1
rough-plaster	0.91	0.75 mm	11.18 m/s	2.5%	-2.0%	1.5%	2
rough-plaster	0.91	0.75 mm	8.94 m/s	1.3%	+0.8%	1.1%	2
rough-plaster	0.91	0.75 mm	6.71 m/s	0.5%	-0.1%	0.4%	3
rough-plaster	0.91	0.75 mm	4.47 m/s	1.7%	-0.9%	1.5%	2
stucco	0.91	1.47 mm	13.41 m/s	6.1%	-6.1%	1.0%	2
stucco	0.91	1.47 mm	11.18 m/s	2.7%	-2.2%	1.6%	3
stucco	0.91	1.47 mm	8.94 m/s	2.6%	+2.2%	1.4%	3
stucco	0.91	1.47 mm	6.71 m/s	6.0%	+5.6%	2.3%	3
stucco	0.91	1.47 mm	4.47 m/s	6.3%	+6.3%	0.6%	2

## 11. Discussion

Developing this theory was difficult due to the lack of photographs of mixed convection streamlines along rough surfaces. Analysis of the measurements made clear that mixed convection from rough plates was different from that of smooth plates. The flow patterns had to be inferred from these measurements and knowledge of natural and forced convections.

Many theories were tried and discarded concerning the forced vertical flow cases. Examination of hypothetical velocity profiles sparked the present theory, which explains the aiding and opposing flow cases both having  $\ell^{\sqrt{3}}$ -norm and  $\ell^3$ -norm asymptotes.

**11.1 Heat Transfer Bounds.** All of the  $\ell^p$ -norms combining natural and forced heat transfer have  $\sqrt{3} \leq p \leq 5$ . The mixed heat transfer is thus bounded between  $\|\overline{h_F}, \overline{h_N}\|_5$  and  $\|\overline{h_F}, \overline{h_N}\|_{\sqrt{3}}$ .

**11.2 Horizontal Flow Obstruction.** The fan pulling air through the chamber is sufficient to counter the effect of the wind-tunnel's obstructions to horizontal flow, except in the case of the vertical plate with opposing flow. In order to draw some air upward at slow (downward) fan speeds, the air's momentum must be reversed. This is modeled by increasing parameter  $B$  of Table 2 by twice the vertical distance from the plate to the test chamber upper edge, normalized by  $L$  and the ratio of the upper edge perimeter to the plate width. This same correction applies to still air in the vertical tunnel.

**11.3 Effective Vertical Reynolds Number.** Aiding and opposing vertical plate measurements in a fluid other than air are needed to further test the effective vertical Reynolds number,  $Re_N$  Formula (9).

**11.4 Rough Velocity Profiles.** The hypothetical forced flows in the Section 6 velocity profiles were turbulent flows. Measurements of both vertical plates in vertical flow conforming to the present theory suggests that the rough and turbulent velocity profiles are similar.

**11.5 Duct Velocity Profile.** The aggregate boiling point kinematic viscosity  $\overline{\nu}_0$  in Formula (22) may be useful in developing formulas for pipe and duct velocity profiles as a function of duct length.

## 12. Conclusions

Formulas were presented for predicting the mixed convective surface conductance of a flat isotropic surface roughness having a convex perimeter in a Newtonian fluid with a steady forced flow in the plane of that roughness.

The prerequisites are the RMS height-of-roughness  $0 < \varepsilon$ , angle  $\theta$  of the surface from vertical, angle  $\psi$  of the forced flow from the zenith,  $Ra/L^3$  and  $Pr$  of the fluid, and the characteristic-length  $L > 0$  and  $Re > 0$  of the forced flow.

- RMS height-of-roughness  $\varepsilon$  is the correct metric for predicting forced convective surface conductance.
- Roughness  $\varepsilon \ll L$  does not affect the natural component of mixed convection.
- Plate inclination does not affect the forced component of mixed convection.
- When  $Re = 0$ , the mixed convection is the same as its natural component.

The present work's formulas were compared with 104 measurements in twelve data-sets from the present apparatus in two inclined and all five corner case orientations. The twelve data-sets had RMSRE values between 1.3% and 4% relative to the present theory.

The present work's formulas were compared with 78 measurements in 28 data-sets on five vertical rough surfaces in horizontal airflow from Rowley et al. [15]. The five stucco data-sets had RMSRE values between 2.5% and 6.5%; the other data-sets had RMSRE values between 0.2% and 5%.

## 13. Nomenclature

$A$	surface area ( $\text{m}^2$ )
$Gr$	Grashof number
$\overline{h}$	average convective surface conductance ( $\text{W}/(\text{m}^2 \cdot \text{K})$ )
$\overline{h}_F$	forced convective surface conductance ( $\text{W}/(\text{m}^2 \cdot \text{K})$ )
$\overline{h}_N$	natural convective surface conductance ( $\text{W}/(\text{m}^2 \cdot \text{K})$ )
$\overline{h}^*$	upward natural convective surface conductance ( $\text{W}/(\text{m}^2 \cdot \text{K})$ )
$\overline{h}'$	vertical plate natural convective surface conductance ( $\text{W}/(\text{m}^2 \cdot \text{K})$ )
$\overline{h}_\theta$	vertical mode of inclined natural convective surface conductance ( $\text{W}/(\text{m}^2 \cdot \text{K})$ )
$\overline{h}'_\theta$	vertical component of $\overline{h}_\theta$ ( $\text{W}/(\text{m}^2 \cdot \text{K})$ )
$\overline{h}_R$	downward natural convective surface conductance ( $\text{W}/(\text{m}^2 \cdot \text{K})$ )
$k$	fluid thermal conductivity ( $\text{W}/(\text{m} \cdot \text{K})$ )
$L$	characteristic length (m)
$L_P$	roughness spatial period (m)
$L^*$	ratio of plate area to its perimeter (m)
$L^\bullet$	ratio of island area to its perimeter (m)
$L_W$	width of plate (m)
$\overline{Nu}$	average Nusselt number
$\overline{Nu}_N$	average Nusselt number of natural convection
$\overline{Nu}'$	average Nusselt number of vertical plate natural convection
$Nu'_0$	Nusselt number of vertical plate conduction
$p$	exponent in $\ell^p$ -norm: $\{ F_1 ^p +  F_2 ^p\}^{1/p}$
$Pr$	Prandtl number of the fluid
$Ra$	Rayleigh number
$Ra'$	vertical plate Rayleigh number
$Ra^*$	upward Rayleigh number
$Ra_R$	downward Rayleigh number
$Re_F$	Reynolds number of the forced flow parallel to the plate
$Re_I$	Reynolds number of rough turbulent transition to forced turbulent flow
$Re_N$	effective Reynolds number of vertical natural convection
$Re_y$	friction Reynolds number

$u(y)$	velocity at $x = L/2$ and distance $y$ from the plate (m/s)
$u_N$	effective natural flow speed $= \nu Re_N/L$ (m/s)
$u^*$	friction velocity (m/s)
$W_0$	principal branch of the Lambert W function
$y$	distance from plate (m)

### 13.1 Greek Symbols.

$\delta$	boundary layer thickness (m)
$\delta_\lambda$	laminar boundary layer thickness (m)
$\delta_\tau$	turbulent boundary layer thickness (m)
$\epsilon$	surface emissivity
$\varepsilon$	surface RMS height-of-roughness (m)
$\eta$	ratio of $Re_N$ and $Re_F$ (either order)
$\kappa$	von Kármán constant $\approx 0.41$
$\Omega$	ratio of non-plateau area to cell area ( $\text{m}^2/\text{m}^2$ )
$\nu$	fluid kinematic viscosity ( $\text{m}^2/\text{s}$ )
$\nu_0$	gas kinematic viscosity ( $\text{m}^2/\text{s}$ ) at boiling point
$\psi$	angle between the forced flow and the zenith; $0^\circ$ is aiding flow; $180^\circ$ is opposing flow
$\theta$	angle of the plate surface from vertical; face up is $-90^\circ$ ; face down is $+90^\circ$
$\Xi$	natural convection self-obstruction factor
$\chi$	roughness velocity correction factor for forced flow
$\chi_I$	plateau islands roughness correction factor

### 13.2 Abbreviations. The following abbreviations are used in this manuscript:

ARM	computer processor architecture
LM35C	temperature sensor integrated circuit
MIC-6 Al	a nearly pure aluminum alloy
MPXH6115A6U	air pressure sensor integrated circuit
PIR	polyisocyanurate foam
RAM	random access memory
RMS	root-mean-squared $\sqrt{\sum_{i=1}^n x_i^2/n}$
RMSRE	root-mean-squared relative error (%)
RSS	root-sum-squared $\sqrt{\sum_{i=1}^n x_i^2}$
STM	STMicroelectronics, an integrated circuit manufacturer
USB	Universal Serial Bus
XPS	extruded polystyrene foam

## Supplementary Materials

A zip archive of PDF files of graphs and estimated measurement uncertainties of each 102-minute time-series producing a convection measurement can be downloaded from:

<http://people.csail.mit.edu/jaffer/convect>

A zip archive of the aggregate measurements are also available from that site.

## Acknowledgments

Thanks to John Cox (1957-2022) and Doug Ruuska for machining the bi-level plate. Thanks to Roberta Jaffer for assistance and problem-solving suggestions. Thanks to anonymous reviewers for their useful suggestions.



#### 14. Appendix A: Velocity Profiles

This investigation assumes that the laminar natural boundary layer thickness  $\delta_\lambda$  is the same as the forced laminar thickness calculated using the effective vertical  $Re_N$ . Formulas from Lienhard and Lienhard [19] lead to natural convection velocity profile  $u(y)$  Formula (38), where  $y$  is the horizontal distance from the mid-line of the vertical plate,  $\nu$  is the fluid's kinematic viscosity, and  $u_N = \nu Re_N/L$  is the effective natural flow speed.

$$u(y) \approx 4 u_N \frac{y}{\delta_\lambda} \left[ 1 - \frac{y}{\delta_\lambda} \right]^2 \quad 0 < y < \delta_\lambda \approx \frac{4.92 L}{\sqrt{Re_N}} \quad (38)$$

In forced turbulent flow along a smooth plate, let friction velocity  $u^* \approx u_\infty \sqrt{\bar{f}_\tau/2}$ , and  $Re_y = u^* y/\nu$ , with  $\bar{f}_\tau$  from Formula (15). Lienhard and Lienhard [19] gives the viscous sublayer velocity profile as Formula (39), and the log-layer velocity profile as Formula (40). The von Kármán constant  $\kappa \approx 0.41$ .

$$\frac{u(y)}{u^*} \approx Re_y \quad Re_y < 7 \quad (39)$$

$$\frac{u(y)}{u^*} \approx \left[ \frac{1}{\kappa} \ln(Re_y) + 5.5 \right] \quad Re_y > 30 \quad (40)$$

Lienhard and Lienhard [19] does not tell how to interpolate these two formulas. The  $7 < Re_y < 30$  range to be interpolated is large, and the transition must be gradual. Adapting the staged-transition formula from Jaffer [2] by using the  $\ell^{-\sqrt{1/3}}$ -norm instead of the  $\ell^{-4}$ -norm in  $Re_Y$  Formula (41) yields Formula (42).

$$Re_Y = \|7, Re_y\|_{-\sqrt{1/3}} \quad y < \delta_\tau \approx \frac{0.37 L}{\sqrt[5]{Re}} \quad (41)$$

$$\frac{u(y)}{u^*} = \left[ 5.5 + \frac{\ln(Re_y)}{\kappa} \right] + \frac{Re_Y}{Re_y} \left[ Re_Y - 5.5 - \frac{\ln(Re_Y)}{\kappa} \right] \quad (42)$$

Formula (43) is a proposed alternative to Formula (42) based on the Lambert  $W_0$  function.

$$\frac{u(y)}{u^*} = \frac{8}{\sqrt{3}} W_0(\sqrt{3} Re_y) \quad (43)$$

The “interpolated” Formula (42) and Formula (43) curves are nearly identical in Figure 28. It is not surprising that a formula for turbulent flow involves the Lambert  $W_0$  function. Formula (43) uses  $W_0(\sqrt{3} Re_y)$  while  $\bar{f}_\tau$  Formula (15) uses  $W_0(Re_F/\sqrt{3})$ .

While interesting, these curves are employed only for estimating the net vertical flow near the plate. None of the convective surface conductance formulas quantitatively depend on them.

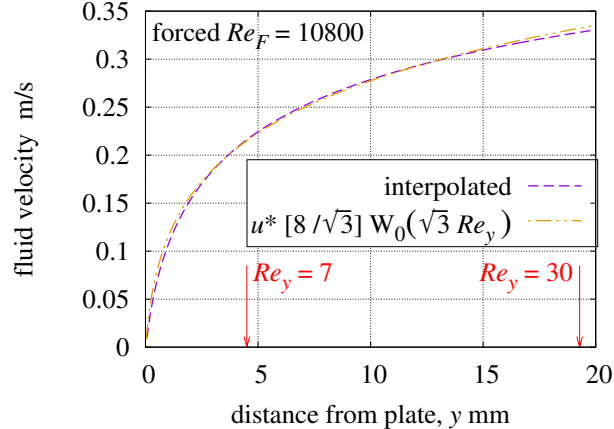


**Figure 28** Forced convection velocity profile

**14.1 Rough Plates.** Because roughness  $\varepsilon \ll L$  has negligible effect on natural convection,  $u_N$  should be the same from smooth and rough plates. Hence, their  $Re_N \equiv u_N \varepsilon / \nu$  should also be equal.

Forced flow along a rough surface traverses a path longer than  $L$ . The effective  $Re_N/Re_F$  ratio of a rough surface should be increased by a function of the “roughness Reynolds number”  $Re_\varepsilon$  Formula (44).

$$Re_\varepsilon = \frac{u^* \varepsilon}{\nu} = \frac{Re}{\sqrt{3} [L/\varepsilon] \ln(L/\varepsilon)} \quad (44)$$

Proposed is  $Re_N/Re$  scale factor  $\chi$  Formula (45), where  $Re$  is the solution of Formula (44) combined with  $Re_\varepsilon = 3 [\varepsilon/L]^2$ . Figure 29 graphs  $\chi$  as a function of  $\varepsilon$ .

$$\chi = \frac{Re_F + Re}{Re_F} = 1 - 3\sqrt{3} \frac{\varepsilon}{L} \ln \frac{\varepsilon}{L} \quad (45)$$

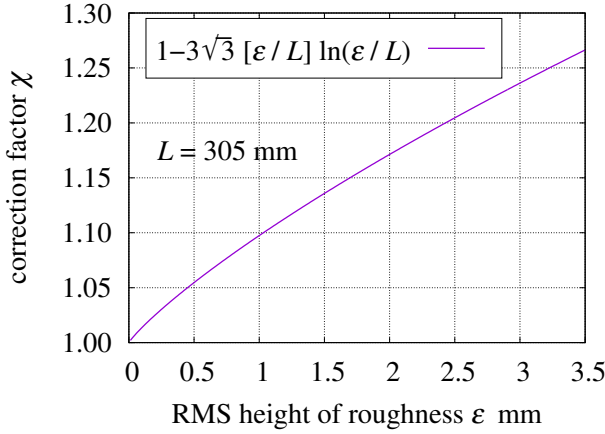


Figure 29  $\chi$  versus  $\varepsilon$

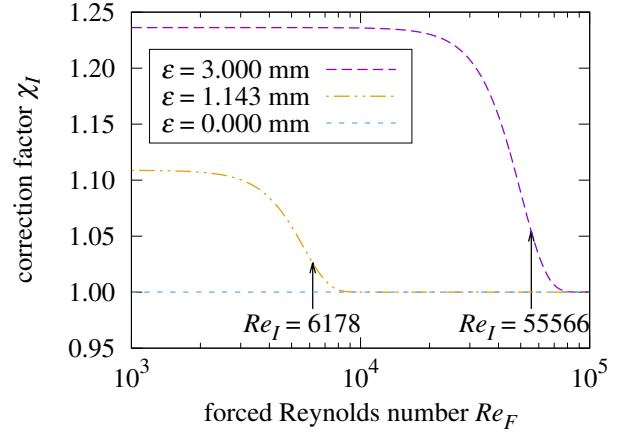


Figure 30  $Re_N$  correction factor  $\chi_I$

## 15. Appendix B: Plateau Islands Roughness Correction

Plates shedding only turbulent flow have  $\chi_I = 1$ . Plates shedding only rough flow have  $\chi_I = \chi$  from Formula (45).

Plateau roughness (forced) convection transitions from rough flow to turbulent flow as the  $\ell^{-4}$ -norm in Formula (18). The scale factor  $\chi_I$  should vary between 1 and  $\chi$  as a function of  $Re_F$ . Expression  $\exp_4(-[Re_F/Re_I]^4)$  varies between 0 and 1. Proposed is  $\chi_I$ , the  $Re_N/Re_F$  scale factor:

$$\chi_I = \exp_\chi(\exp_4(-[Re_F/Re_I]^4)) \quad (46)$$

Note the similarity of Formula (46) and Formula (27) with  $\zeta = 4$ .

Figure 30 plots  $\chi_I$  with  $\varepsilon = 3$  mm,  $\varepsilon = 1.143$  mm, and  $\varepsilon = 0$ .

## 16. Appendix C: Apparatus and Measurement Methodology

The original goal of the present apparatus was to measure forced convection heat transfer from a precisely rough plate over the widest practical span of airflow velocities. To minimize natural convection, it measured downward natural convection mixed with horizontal forced flow. Its measurements are presented in Jaffer [2].

Although more complicated to analyze, the plate was suspended, not embedded, in the wind-tunnel. The measurements from prior investigations which embedded the plate in a wind-tunnel wall were largely incompatible with the present theory because their flows were not isobaric.

The small size of the wind-tunnel chassis (1.3 m  $\times$  0.61 m  $\times$  0.65 m) afforded an opportunity to characterize mixed convection at other orientations of the plate and flow.

**16.1 The Plate.** Figure 31 shows the rough surface of the test plate; it was milled from a slab of MIC-6 aluminum (Al) to have (676 of) square 8.33 mm  $\times$  8.33 mm  $\times$  6 mm posts spaced on 11.7 mm centers over the 30.5 cm  $\times$  30.5 cm plate. The area of the top of each post was 0.694 cm<sup>2</sup>, which was 50.4% of its 1.38 cm<sup>2</sup> cell. The RMS height-of-roughness  $\varepsilon = 3.00$  mm. Openness  $\Omega \approx 49.6\%$ . Embedded in the plate are 9 electronic resistors as heating elements and a Texas Instruments LM35 Precision Centigrade Temperature Sensor. 2.54 cm of thermal insulating foam separates the back of the plate from a 0.32 mm thick sheet of aluminum with an LM35 at its center. Figure 32 is a cross-section illustration of the plate assembly.

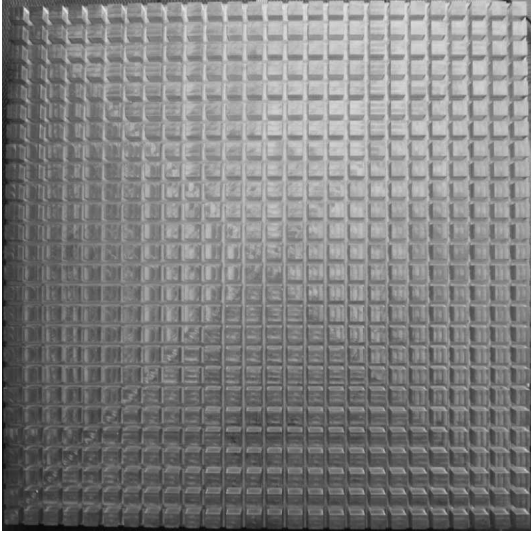


**Figure 31** Rough surface of plate

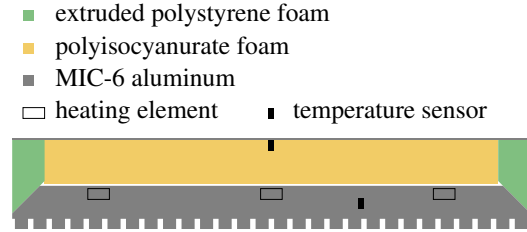


**Figure 32** Plate assembly cross-section

**16.2 Wind Tunnel.** The fan pulls air from the test chamber's open intake through the test chamber. The fan blows directly into a diffuser made of folded plastic mesh to disrupt vortexes generated by the fan. In a sufficiently large room, the disrupted vortexes dissipate before being drawn into the open intake.

To guarantee isobaric (no pressure drop) flow, the wind-tunnel must be sufficiently large that its test chamber and plate assembly boundary-layers do not interact at fan-capable airspeeds.

The wind-tunnel test chamber in Figure 33 has a 61 cm  $\times$  35.6 cm cross-section and a 61 cm depth. This allows the plate assembly to be centered in the wind-tunnel with 15 cm of space on all sides. The fan pulling air through the test chamber produces a maximum airspeed of 4.65 m/s ( $Re \approx 9.2 \times 10^4$  along the 30.5 cm square plate). Its minimum nonzero airspeed is 0.12 m/s ( $Re \approx 2300$ ).

Test chamber laminar and turbulent 99% boundary-layer thicknesses (Schlichting [7]) are:

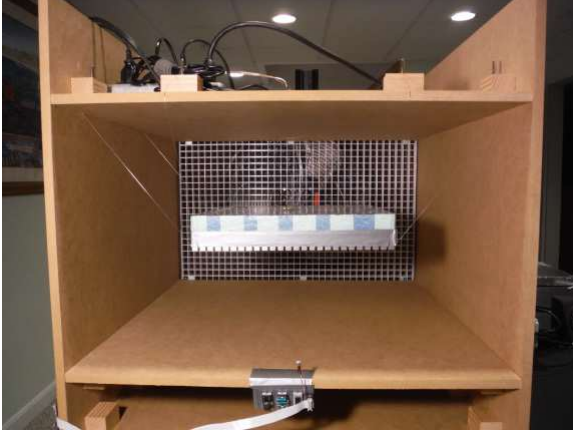
$$\delta_\lambda = 4.92 \sqrt{\frac{x\nu}{u}} \quad \delta_\tau = 0.37 x^{4/5} \left[ \frac{\nu}{u} \right]^{1/5} \quad (47)$$

Figure 34 shows that the 15 cm clearance between the plate and the test chamber walls is sufficient to prevent their boundary-layers from interacting at airspeeds within the fan's capabilities.

The plate assembly (face down in Figures 32 and 33) is suspended by six lengths of 0.38 mm-diameter steel piano wire terminated at twelve zither tuning pins in wooden blocks fastened to the exterior of the test

chamber. With the plate assembly in the test chamber, the airspeed increases in proportion to the reduction of test chamber aperture  $A_e$  by the plate's cross-sectional area  $A_x$ :

$$\frac{u_x}{u} = \frac{A_e}{A_e - A_x} \approx 107.6\% \quad (48)$$



**Figure 33**  $\varepsilon = 3$  mm plate in wind-tunnel

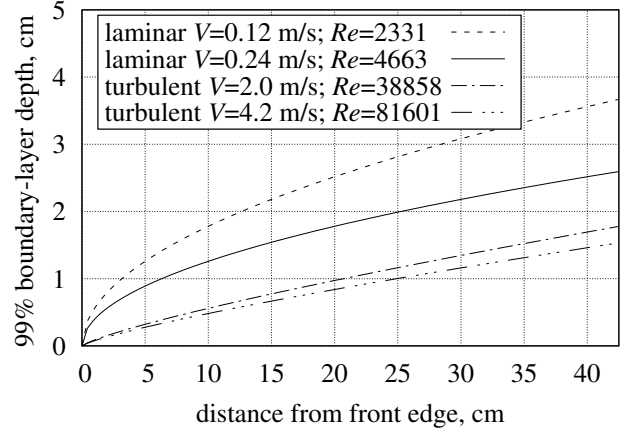


**Figure 34** Wind-tunnel boundary-layers

**16.3 Automation.** Data capture and control of convection experiments are performed by an “STM32F3 Discovery 32-Bit ARM M4 72MHz” development board. The program written for the STM32F3 captures readings and writes them to the microprocessor’s non-volatile RAM, controls the plate heating, servos the fan speed, and later uploads its data to a computer through a USB cable.

Once per second during an experiment, the program calibrates and reads each on-chip 12 bit analog-to-digital converter 16 times, summing the sixteen 12 bit readings to create a 16 bit reading per converter.

Rotations of the fan are sensed when a fan blade interrupts an infrared beam. The microprocessor controls a solid-state relay (supplying power to the fan) to maintain a fan rotation rate,  $\omega$ , which is dialed into switches. At  $\omega \leq 210$  r/min, the microprocessor pulses power to the fan to phase-lock the beam interruption signal to an internal clock. At  $\omega > 210$  r/min, the microprocessor servos the duty cycle of a 7.5 Hz square-wave gating power to the fan. This system operates at  $32 \text{ r/min} < \omega < 1400 \text{ r/min}$ .

**16.4 Calibration.** The correspondence between fan rotation rate  $\omega$  and test chamber airspeed  $u$  was determined using an “Ambient Weather WM-2”, which specifies an accuracy of  $\pm 3\%$  of reading. After 2017 an “ABM-200 Airflow & Environmental Meter” specifying an accuracy of  $\pm 0.5\%$  of reading between 2.2 m/s and 62.5 m/s, was used.

The “UtiliTech 20 inch 3-Speed High Velocity Floor Fan” has three blades with maximum radius  $r = 0.254$  m. Its characteristic length is its hydraulic-diameter,  $D_H = 0.550$  m. The velocity of the blade tips is  $2\pi r\omega/60$ , where  $\omega$  is the number of rotations per minute. The Reynolds number of the fan is:

$$Re_f = \frac{2\pi r D_H \omega / 60}{3\nu} \quad (49)$$

The 3 blade tips trace the whole circumference in only 1/3 of a rotation, hence the 3 in the denominator.

Faster fan rotation  $\omega$  yields diminishing increases of test-chamber airspeed  $u_t$ , suggesting Formula (50), where  $u_u$  is the limiting velocity for arbitrarily fast rotation, and coefficient  $\eta$  converts fan  $Re_f$  to test-chamber  $Re_t$ . Figure 35 gives the parameters and measurements at  $300 \text{ r/min} \leq \omega \leq 1500 \text{ r/min}$ . The “3mm” points are the WM-2 measurements of the 3 mm plate in the original wind-tunnel; The “1mm” points are the ABM-200 measurements of the 1 mm plate in the tunnel with a new diffuser and fan cowl.

$$Re_t = \|\eta Re_f, D_H u_u / \nu\|_{-2} \quad u_t = \|\pi \eta r \omega / 90, u_u\|_{-2} \quad (50)$$

Airspeeds slower than 2 m/s should be nearly proportional to  $\omega$ . Both anemometers show evidence of dry (bearing) friction in Figure 35. The ABM-200 “meter predictions” trace plots  $1.125 u_t - 0.381$ ; the

WM-2 “meter predictions” trace plots  $1.477 u_t - 0.81$  when  $u_t < 1.725$  and  $u_t$  otherwise. A mistake in the 2016 measurement software under-counted fan rotations at  $\omega > 1200$  r/min. It is compensated by replacing  $\omega$  in Formulas (49, 50) with  $[\omega^{-6} - 1750^{-6}]^{-1/6}$  in the WM-2 “meter predictions”. The RMSRE and Bias are relative to the “meter predictions”. The second “1mm” row includes the point at 400 r/min.

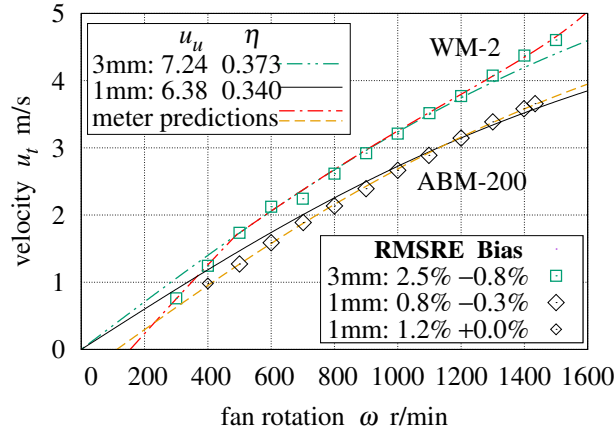


**Figure 35** Airspeed versus fan speed

Figures 36 and 37 show the fan speed variability in each experiment; these are used in the measurement uncertainty calculations.

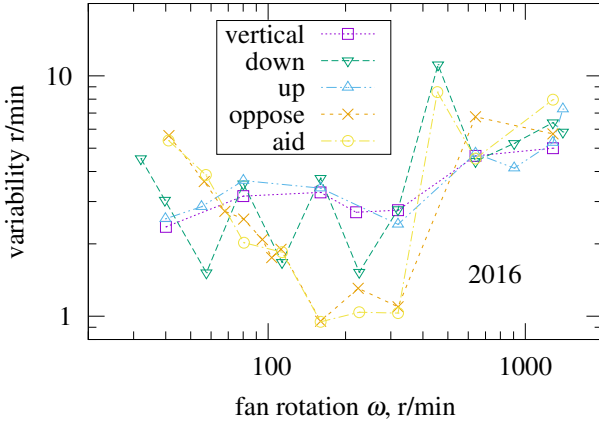


**Figure 36** Fan variability 3 mm plate

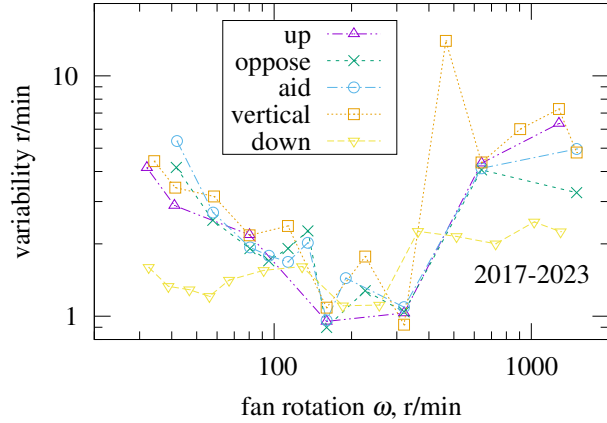


**Figure 37** Fan variability 1 mm plate

**16.5 Ambient Sensing.** Figure 38 shows the ambient sensor board which was at the lower edge of the test chamber in Figure 33. It measures the pressure, relative humidity, and air temperature at the wind-tunnel intake. Wrapped in aluminum tape to minimize radiative heat transfer, the LM35 temperature sensor projects into the tunnel. To minimize self-heating, the LM35 is powered only while being sampled.

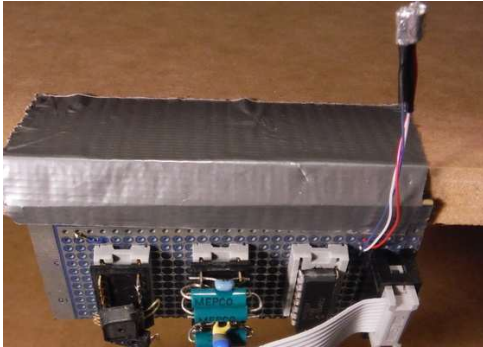


**Figure 38** Ambient sensors

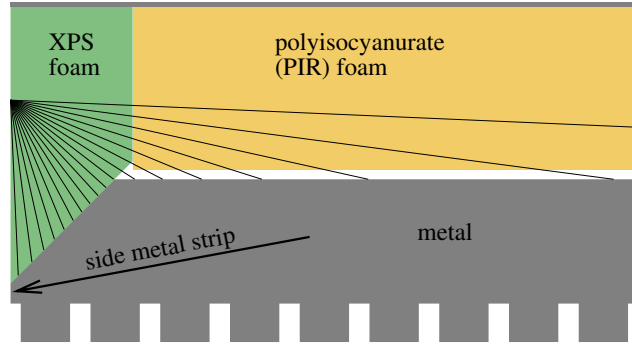


**Figure 39** XPS wedge conduction

**16.6 Physical Parameters.** Table 9 lists the static parameters from measurements and specifications.

The effective  $\epsilon_{wt}$  may differ from the medium-density-fiberboard emissivity given by Rice [20] because the temperatures of the test chamber surfaces may not be uniform. Through the open intake, the plate also exchanges thermal radiation with objects in the room having different temperatures.

**Table 9 Physical parameters**

Symbol	Values	Description
$L$	0.305 m	length of flow along test-surface
$A$	0.093 m <sup>2</sup>	area of test-surface
$\epsilon$	3.00 mm    1.04 mm	RMS height-of-roughness
$C_{pt}$	4691 J/K    4274 J/K	plate thermal capacity
$D_{Al}$	19.4 mm	metal slab thickness
$D_{PIR}$	25.4 mm	polyisocyanurate (PIR) foam thickness
$D_w$	19.05 mm	XPS foam wedge height
$k_{PIR}$	0.0222 W/(m · K)	PIR foam thermal conductivity
$k_{XPS}$	0.0285 W/(m · K)	XPS foam thermal conductivity
$U_I$	0.075 W/K	front-to-back insulation thermal conductance
$\epsilon_{Al}$	0.04	test-surface (MIC-6 Al) emissivity
$\epsilon_{XPS}$	0.515	XPS foam emissivity (see text)
$\epsilon_{dt}$	0.89	duck tape emissivity
$\epsilon_{wt}$	0.90	test chamber interior emissivity

**16.7 The 1 mm Roughness Plate.** When the 6 mm posts were milled down to 2 mm height, the four corner posts were left at their 6 mm height in order to preserve the wire suspension. This resulted in  $\epsilon = 1.04$  mm for the plate as a whole. However,  $Re_I$  occurs within the first few rows of posts.  $\epsilon = 1.143$  mm over the first three rows of posts results in  $Re_I = 6178$ .

**16.8 Modeling of Parasitic Heat Flows.** The plate has six surfaces from which heat can flow. At low airflow velocities, the sides of the insulation behind the test plate can leak more heat than the test-surface transfers, shrinking to 6% at 1300 r/min.

In order to measure natural convection from the (rough) test surface, natural convection and thermal radiation from the four sides ( $U_S$ ) and back must be deducted from the total heat flow. Heat from the front plate flows through thermal insulating foam to a thin aluminum sheet with a temperature sensor at its center. This heat flow is simply  $U_I [T_P - T_B]$ , the product of the foam's thermal conductance and the temperature difference across it.

**16.9 Forced Convection Side Model.** The four sides are not isothermal; a 3.5 mm metal strip (see cross-section Figure 39) runs the length of the side; and a  $D_w$ -tall wedge of extruded polystyrene foam (XPS) insulation fills the metal slab's 27 mm ( $= \sqrt{2} D_{Al}$ ) 45° chamfer. The local surface conductance  $h_W(z)$  at elevation  $z$  (from the wedge point) is found by averaging the reciprocal distance to slab metal with respect to angle  $\theta$ :

$$\begin{aligned}
h_W(z) &= \int_0^{\theta_c} \frac{k_{XPS}}{\sqrt{2} z \theta_c} \cos\left(\theta + \frac{\pi}{4}\right) d\theta + \int_{\theta_w}^{\theta_W} \frac{k_{PIR}}{z - D_w} \frac{\cos \theta}{\theta_W - \theta_w} d\theta \\
&= \frac{k_{XPS}}{\sqrt{2} z \theta_c} \left[ \sin\left(\theta_c + \frac{\pi}{4}\right) - \sin \frac{\pi}{4} \right] + \frac{k_{PIR}}{z - D_w} \left[ \frac{\sin \theta_W - \sin \theta_w}{\theta_W - \theta_w} \right] \\
\theta_c &= \arctan \frac{D_w - z}{D_w} \quad \theta_w = \arctan \frac{D_w}{z - D_w} \quad \theta_W = \max\left(\theta_w, \arctan \frac{L - D_w}{z - D_w}\right)
\end{aligned} \tag{51}$$

Forced air flows parallel to the long dimension on two sides, but flows into the windward side and away from the leeward side. Air heated by the windward side reduces heat transfer from the test-surface; air heated by the test-surface suppresses heat transfer from the leeward side. Hence, the model excludes windward and leeward forced convection. The average forced convective conductance of the flow-parallel foam wedges is calculated by integrating  $h_W(z)$  in series (reciprocal of the sum of reciprocals, which is also the  $\ell^{-1}$ -norm) with the local surface conductance  $k Nu_\sigma(Re_x)/L$ , where  $Nu_\sigma(Re_x)$  is the local pierced-laminar convection

from Jaffer [2]:

$$U_W = \int_0^{D_w} \int_0^L \left\| h_W(z), \frac{k Nu_\sigma(Re_x)}{L} \right\|_{-1} dx dz \quad (52)$$

**16.10 Other Side Models.** The heat flow through the four sides  $U_S$  will be estimated from the plate and ambient temperatures. While the forced convective surface conductance of the sides is modeled by integrating the local forced surface conductance, this is not generally possible for natural convection.

Natural convection formulas are known for some convex surfaces. The plate’s side metal surface is not convex.

Instead, the effective side width  $L_{es}$  and effective emissivity  $\epsilon_W$  are introduced into the model. The natural convection of each side is calculated for an  $L_{es} \times L_C$  area instead of its actual  $L_S \times L_C$  area. The black-body radiation from each side is calculated for its actual  $L_S \times L_C$  area with an effective emissivity of  $\epsilon_W$ .

The flow patterns in Fujii and Imura [3] figures 14(e) and 14(f) (and schematic drawing Figure 2) show a plume rising from the center of an upward-facing plate fed by flow from the plate’s edges. For the test surface, the upward heat flow of 0.467 W/K is more than twice the 0.212 W/K expected from the back and sides. Convective flow from the upward-facing test surface will draw in the air heated by the back and sides, reducing heat transfer from the test surface. In order to avoid double counting the convected heat from the back and sides, they should not be deducted from the plate heat (the thermal radiation is still deducted). The “reuptake” of this convected back and side heat should be nearly complete; its coefficient was set to 1 to avoid introducing another degree-of-freedom into the model.

Not deducting side convection from upward natural convection has an unexpected benefit: the upward convection model is thus insensitive to  $L_{es}$ , allowing  $\epsilon_W$  to be determined from only upward-facing measurements.

**16.11 Radiative Transfer Side Model.** The 3 mm roughness plate had its sides wrapped with duck tape, which has a different emissivity from the foam wedges forming each side surface. Some of the 1 mm roughness plate runs were with tape and some without, requiring different  $\epsilon_W$  values. For taped sides  $\epsilon_W \approx 0.703$ ; without tape  $\epsilon_W \approx 0.515$ .

Figure 33 shows duck tape applied to the lower 54% of the plate’s side, which corresponds to 50% coverage of the XPS foam wedge. For this partial tape coverage,  $\epsilon_W$  Formula (53) is the area proportional mean of the duck tape emissivity and XPS emissivity. Barreira, Almeida, and Simões [21] measured  $\epsilon_{dt}$  emissivities of 0.86 and 0.89 from two brands of “duck tape”. The emissivity is largely controlled by the exposed polyethylene film, and increases with oxidation. Hence, the larger value is used for the aged duck tape on the plate sides. As of this writing, published emissivity measurements of XPS foam have not been located.

$$\epsilon_W = 50\% \epsilon_{dt} + 50\% \epsilon_{XPS} \quad (53)$$

Natural convection measurements ( $u = 0$ ) from the plate assembly over the span of inclinations in Figure 4 have less than 3.3% RMSRE when calculated with  $\epsilon_{XPS} = 0.515$ ; the RMSRE increases to either side of 0.515. This value is consistent with natural convection measurements of the plate assembly without tape.

**16.12 Natural Convection Side Model.** With  $\epsilon_W$  thus determined,  $L_{es}$  was the remaining degree of freedom. Trials with vertical and downward plate measurements found that  $L_{es}$  had a value near the sum of the aluminum slab thickness 19.4 mm and the effective height of the side face of the roughness  $\approx \sqrt{2}\epsilon$ . This makes sense for a natural convection dimension; it is used for  $L_{es}$ . The 3 mm roughness plate has  $L_{es} \approx 23.6$  mm; 1 mm has  $L_{es} \approx 21.0$  mm.

In the vertical case, 1/2 of the heated air from the bottom side flows along the vertical test surface and would be counted twice. And 1/2 of the air drawn by the top side comes from the vertical test surface and would be counted twice. This vertical reuptake coefficient was set to 1/2; discrepancy from the actual reuptake coefficient will manifest as error in measurements.

Consider the (initially) vertical plate as  $\theta$  decreases from  $0^\circ$ . As the bottom side face tilts upward, more (than half of the) heated air will rise toward the test surface. That heat will reduce the convection from the

test surface. When tilted downward, the heat from the test surface will reduce the convection from the top side. To handle these cases, Equation (54) includes a term  $2 \cos \theta \sin \theta$  whose minimum of  $-1$  is reached at  $\theta = -45^\circ$  and a term  $-2 \cos \theta \sin \theta$  whose minimum of  $-1$  is reached at  $\theta = +45^\circ$ .

**16.13 Combining Radiative Transfer and Convection.** A side's radiative emissions,  $U_\epsilon$ , compete with its convective heat transfer. Both increase with side temperature, but both act to lower that side temperature. Competitive heat transfer processes can often be modeled using the  $\ell^p$ -norm with  $p > 1$ . The value of  $p$  was adjusted so that the  $\Delta T = 3.8\text{K}$  and  $\Delta T = 11\text{K}$  data points align with the theory traces in Figure 4. The optimal range is between  $p = 4/3$  and  $p = 3/2$ ; the geometric mean of those values is  $p = \sqrt{2}$ . The  $\ell^{\sqrt{2}}$ -norm appears three times in  $U_S$  Formula (54).

Formula (54)  $U_S$  is an amount which will be deducted from the measured heat flow. For each side, the  $\ell^{\sqrt{2}}$ -norm of the radiative and convective conductances is paired with the product of the convective conductance and a continuous trigonometric function of  $\theta$  which goes negative when the natural convection would otherwise be double counted. Because of the triangle inequality, the  $\ell^{\sqrt{2}}$ -norm will be greater than the convective component; thus, each side's contribution to  $U_S$  will be positive.

No more than one reuptake process will be simultaneously active for a side. In Formula (54), the expressions  $\min(0, \sin \theta, -.5 \cos \theta, 2 \cos \theta \sin \theta)$  and  $\min(0, \sin \theta, -.5 \cos \theta, -2 \cos \theta \sin \theta)$  return the negative of the largest magnitude potential reuptake. Table 10 describes the natural convection parameters and function.

Note that this analysis applies only to the plate assembly in alignment with the wind-tunnel, and oriented to have at least one horizontal edge. Hence, rotation in plane of plate,  $\phi$ , must be an integer multiple of  $90^\circ$ . The only effect of  $\phi$  in the equations is to swap arguments  $L_F$  and  $L_W$  when  $\phi$  is an odd multiple of  $90^\circ$ .

**Table 10 Natural convection function and parameters**

Symbol	Description
$U_N(\theta, L_F, L_W, \phi)$	natural convective conductance from Jaffer [5]
$\theta$	surface angle from vertical ( $-90^\circ$ is face up)
$L_F$	plate length
$L_W$	plate width
$\phi$	rotation in plane of plate; integer multiple of $90^\circ$
$L_C = 0.305 \text{ m}$	plate length = side length
$L_S = 45.8 \text{ mm}$	side width
$L_{es} = 19.4 \text{ mm} + \sqrt{2} \epsilon$	effective side width for natural convection
$\epsilon_{wt} = 0.9$	wind-tunnel test chamber emissivity
$\epsilon_W \approx 0.703$ taped; $0.515$ bare	effective side emissivity
$h_R$	black-body radiative surface conductance
$U_\epsilon = L_C L_S \epsilon_W \epsilon_{wt} h_R$	radiative emission from a side

$$\begin{aligned}
U_S = & \|U_\epsilon, U_N(\theta - 90^\circ, L_C, L_{es}, 0^\circ)\|_{\sqrt{2}} \\
& + U_N(\theta - 90^\circ, L_C, L_{es}, 0^\circ) \min(0, \sin \theta, -.5 \cos \theta, -2 \cos \theta \sin \theta) \\
& + \|U_\epsilon, U_N(90^\circ - \theta, L_C, L_{es}, 0^\circ)\|_{\sqrt{2}} \\
& + U_N(90^\circ - \theta, L_C, L_{es}, 0^\circ) \min(0, \sin \theta, -.5 \cos \theta, 2 \cos \theta \sin \theta) \\
& + 2 \|U_\epsilon, U_N(0^\circ, L_{es}, L_C, \theta)\|_{\sqrt{2}} \\
& + 2 U_N(0^\circ, L_{es}, L_C, \theta) \min(0, \sin \theta)
\end{aligned} \tag{54}$$

$U_{B0}$  is the test surface reuptake conductance from the back. Its  $\min(0, \sin \theta)$  term is squared because the heated air from the back must flow around two right-angle edges to reach the test surface.

$$U_{B0} = -U_N(90^\circ, L_C, L_C, 0^\circ) \min(0, \sin \theta)^2 \tag{55}$$



Figures 40, 41, and 42 show upward, vertical, and downward convection measurements, respectively. Taken from 3 mm and 1 mm roughness plates over a range of  $Ra$  values, these graphs, in combination with Figure 4 test the natural convection and radiative transfer side models.

The traces labeled “theory” are Formula (7) with the appropriate row of Table 2. The difference between  $\psi = 0^\circ$  and  $\psi = 180^\circ$  in Figure 41 is explained in Section 11.

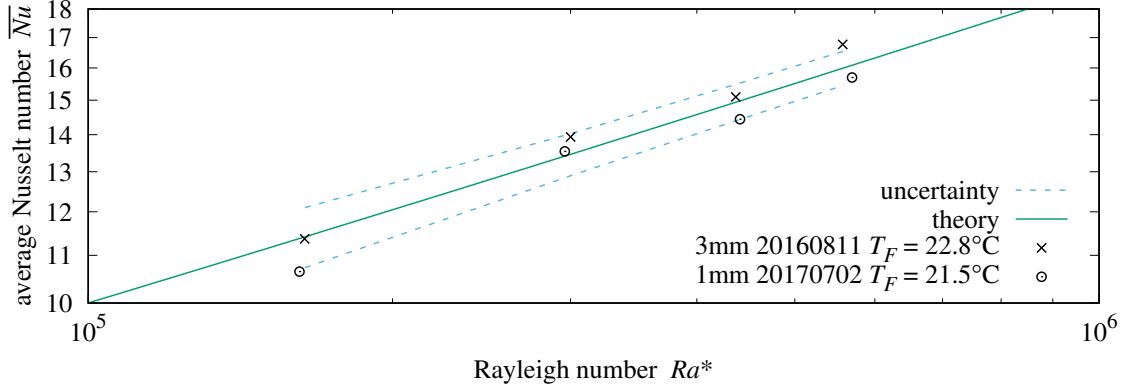


Figure 40 Natural convection from upward-facing surface

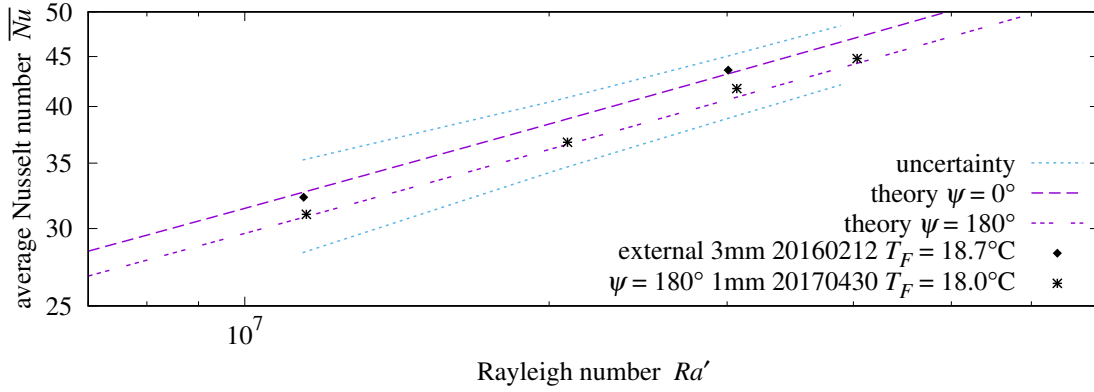


Figure 41 Natural convection from vertical surface

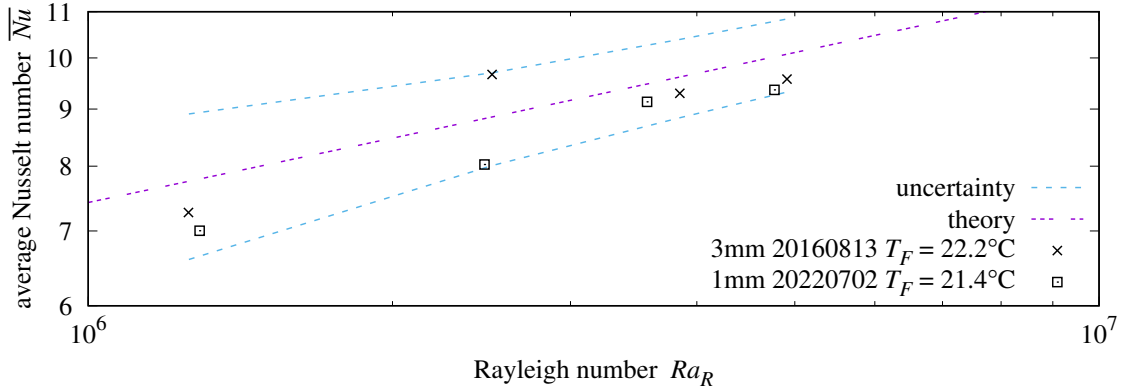


Figure 42 Natural convection from downward-facing surface

**16.14 Mixed Convection Side Model.** Each  $\ell\sqrt{2}$ -norm instance of a call to  $U_N$  is replaced by a call to  $U_M$ , with first argument  $U_{fl}(u)$  or  $U_{ft}(u)$ . In order to ignore forced convection from the leading and trailing sides,  $U_{ft}(u) = 0$  when  $\psi = 90^\circ$  (horizontal flow); otherwise,  $U_{fl}(u) = 0$ .

The reuptake instances of  $U_N(\theta, L_F, L_W, \phi)$  are changed to the equivalent  $U_M(0, \theta, L_F, L_W, \phi, 0^\circ)$ .

**Table 11 Mixed conductance functions and parameters**

Symbol	Description
$U_{fl}(u)$	level flow side forced thermal conductance
$U_{ft}(u)$	tilted flow side forced thermal conductance
$u$	bulk flow velocity
$U_M(U_F, \theta, L_F, L_W, \phi, \psi)$	mixed convective conductance
$U_F$	forced thermal conductance
$\theta$	surface angle from vertical ( $-90^\circ$ is face up)
$L_F$	forced characteristic length
$L_W$	other plate dimension
$\phi$	rotation in plane of plate; integer multiple of $90^\circ$
$\psi$	angle of fluid flow from vertical ( $0^\circ$ is upward)

$$\begin{aligned}
U_S(u) = & \|U_\epsilon, U_M(U_{fl}(u), \theta - 90^\circ, L_C, L_{es}, 0^\circ, \psi)\|_{\sqrt{2}} \\
& + U_M(0, \theta - 90^\circ, L_C, L_{es}, 0^\circ, 0^\circ) \min(0, \sin \theta, -.5 \cos \theta, -2 \cos \theta \sin \theta) \\
& + \|U_\epsilon, U_M(U_{fl}(u), 90^\circ - \theta, L_C, L_{es}, 0^\circ, \psi)\|_{\sqrt{2}} \\
& + U_M(0, 90^\circ - \theta, L_C, L_{es}, 0^\circ, 0^\circ) \min(0, \sin \theta, -.5 \cos \theta, 2 \cos \theta \sin \theta) \\
& + 2 \|U_\epsilon, U_M(U_{ft}(u), 0^\circ, L_{es}, L_C, \theta, \psi)\|_{\sqrt{2}} \\
& + 2 U_M(0, 0^\circ, L_{es}, L_C, \theta, 0^\circ) \min(0, \sin \theta)
\end{aligned} \tag{56}$$

When  $u$  is large,  $U_S(u)$  approaches the sum of the forced convection conductances.  $U_S(0) \equiv U_S$  of Formula (54).

**16.15 Measurement Methodology.** The measurement methodology employed is unusual. Instead of waiting until the plate reaches thermal equilibrium, the plate is heated to 15 K above ambient, heating stops, the fan runs at the designated speed, and convection cools the plate. All of the sensor readings are captured each second during the 102 minute process, Table 12 lists the dynamic physical quantities measured each second. Table 13 lists computed quantities. Both  $U_S(u)$  and  $\{\epsilon_{Al} \epsilon_{wt} h_R A\}$  are subtracted from the combined heat flow. The mean of  $\bar{h}(u, t)$  over the time interval in which  $\Delta T$  drops by half (or exceeds 6142 s total time) is the result from that experiment.

**Table 12 Dynamic quantities**

Symbol	Units	Description
$\omega$	r/min	fan rotation rate
$T_F$	K	ambient air temperature
$T_P$	K	plate temperature
$T_B$	K	back surface temperature
$P$	Pa	atmospheric pressure
$\Phi$	Pa/Pa	air relative humidity

**Table 13 Computed quantities**

Symbol	Units	Description
$h_R$	W/(m <sup>2</sup> K)	radiative surface conductance
$U_S(u)$	W/K	side radiative and convective conductance
$\bar{h}(u, t)$	W/(m <sup>2</sup> K)	convective surface conductance

**16.16 Heat Balance.** Collecting into  $U_T(u)$  Formula (57) those terms which have a factor of temperature difference  $\overline{T_P} - \overline{T_F}$ , Formula (58) is the heat balance equation of the plate during convective cooling:

$$U_T(u) = U_S(u) + \{\overline{h}(u) A\} + \{\epsilon_{Al} \epsilon_{wt} h_R A\} \quad (57)$$

$$0 = U_T(u) [\overline{T_P} - \overline{T_F}] + U_I [\overline{T_P} - \overline{T_B}] + C_{pt} \frac{d\overline{T_P}}{dt} \quad (58)$$

The plate and ambient temperatures are functions of time  $t$ . Determined experimentally during heating, the temperature group-delay through the 2.54 cm block of insulation between the slab and back sheet is 110 s:

$$\overline{T_P}(t) = \frac{U_T(u) \overline{T_F}(t) + U_I \overline{T_B}(t - 110 \text{ s}) - C_{pt} [d\overline{T_P}(t)/dt]}{U_T(u) + U_I} \quad (59)$$

To compute Nusselt number  $\overline{Nu} = \overline{h} L/k$ , Equation (59) is solved for the  $\{\overline{h}(u, t) A\}$  term from Equation (57).

$$\varsigma(t) = -U_I [\overline{T_P}(t) - \overline{T_B}(t - 110 \text{ s})] \quad (60)$$

$$\{\overline{h}(u, t) A\} = \frac{\varsigma(t) - C_{pt} [\overline{T_P}(t) - \overline{T_P}(t')]/[t - t']}{\overline{T_P}(t) - \overline{T_F}(t)} - \{\epsilon_{Al} \epsilon_{wt} h_R A\} - U_S(u) \quad (61)$$

where  $t'$  is the previous value of  $t$ . In Equations (60) and (61),  $\overline{T_P}(t)$ ,  $\overline{T_F}(t)$ , and  $\overline{T_B}(t)$  are the 15-element cosine averages of plate and fluid temperatures (centered at time  $t$ ).

In order to simulate  $T_P$  from the other dynamic inputs, (59) is solved as a finite-difference equation where  $dt = t - t' = 1$ :

$$T_P(t) = \frac{U_T(u) \overline{T_F}(t) + U_I \overline{T_B}(t - 110 \text{ s}) + C_{pt} T_P(t')}{U_T(u) + U_I + C_{pt}} \quad (62)$$

In Equation (62),  $T_P(t')$  is the previous simulated value, not a measured value.

**16.17 Measurement Uncertainty.** Following Abernethy, Benedict, and Dowdell [22], the final steps in processing an experiment's data are:

- 1) Using Equation (61), calculate the sensitivities of convected power  $\overline{h} A \Delta T$  per each parameter's average over the measurement time-interval;
- 2) multiply the absolute value of each sensitivity by its estimated parameter bias to yield component uncertainties;
- 3) calculate combined bias uncertainty as the root-sum-squared (RSS) of the component uncertainties;
- 4) calculate the RSS combined measurement uncertainty as the RSS of the combined bias uncertainty and twice the product of the rotation rate sensitivity and variability.

Tables 14 and 15 list the sensitivity, bias, and uncertainty for each component contributing more than 0.20% uncertainty for downward-facing 3 mm and 1 mm roughness plates, respectively. Figures 43 and 44 show the measurements relative to the present theory for rough flow and turbulent flow, respectively.

The supplementary data contains these graphs and tables for each data-set.

**Table 14 Estimated measurement uncertainties, bi-level 3mm roughness at  $Re = 59593$ .**

Symbol	Nominal	Sensitivity	Bias	Uncertainty	Component
$\Delta T$	9.47K	+12.2%/K	0.10K	1.22%	LM35C differential
$P$	101kPa	+0.0009%/Pa	1.5kPa	1.28%	MPXH6115A6U air pressure
$C_{pt}$	4.69kJ/K	+0.024%/(J/K)	47J/K	1.13%	plate thermal capacity
$\eta$	0.401	+180%	0.014	2.52%	anemometer calibration
$\varsigma$	6.00mm	+11285%/m	100um	1.13%	post height
				3.49%	combined bias uncertainty
Symbol	Nominal	Sensitivity	Variability	Uncertainty	Component
$\omega$	905r/min	+0.081%/(r/min)	5.2r/min	0.43%	fan rotation rate
				3.60%	RSS combined uncertainty

**Table 15 Estimated measurement uncertainties, bi-level 1mm roughness at  $Re = 55935$ .**

Symbol	Nominal	Sensitivity	Bias	Uncertainty	Component
$\Delta T$	10.2K	+11.7%/K	0.10K	1.17%	LM35C differential
$P$	100.0kPa	+0.0008%/Pa	1.5kPa	1.26%	MPXH6115A6U air pressure
$C_{pt}$	4.24kJ/K	+0.028%/(J/K)	42J/K	1.17%	plate thermal capacity
$\eta$	0.340	+195%	0.003	0.66%	anemometer calibration
$u_u$	6.381	+2.44%	0.100	0.24%	diffuser airflow upper bound
$L_T$	8.34mm	+9365%/m	100um	0.94%	post length
$L_m$	3.57mm	+454%/m	500um	0.23%	side metal strip width
$\epsilon_{rs}$	0.040	+20.4%	0.010	0.20%	test-surface emissivity
$\epsilon_{wt}$	0.900	+9.05%	0.025	0.23%	wind-tunnel emissivity
				2.44%	combined bias uncertainty
Symbol	Nominal	Sensitivity	Variability	Uncertainty	Component
$\omega$	1.03kr/min	+0.065%/(r/min)	2.5r/min	0.16%	fan rotation rate
				2.46%	RSS combined uncertainty

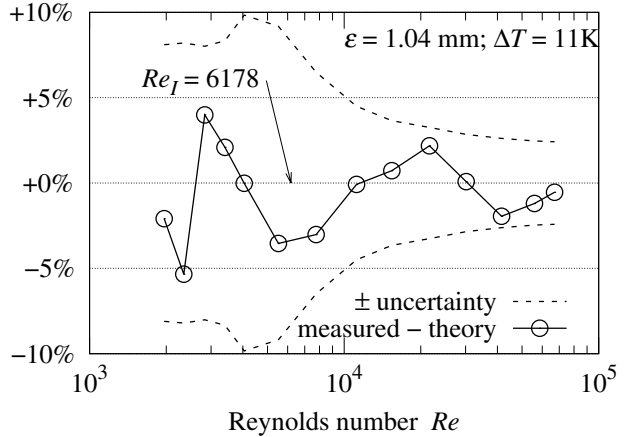
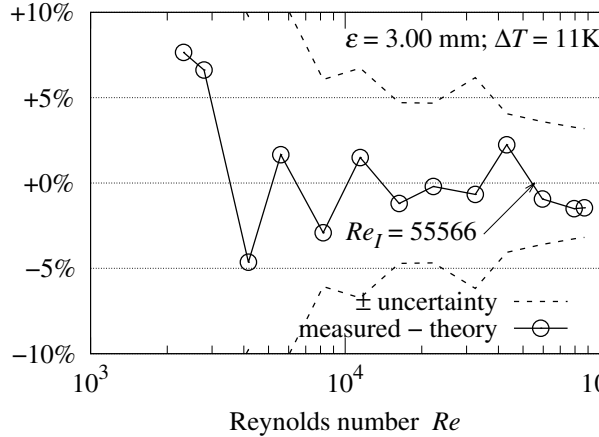


**Figure 43 Measured versus theory  $\epsilon = 3$  mm Figure 44 Measured versus theory  $\epsilon = 1$  mm**

16.18 **Details.** Documentation, photographs, electrical schematics, and software source-code for the apparatus, as well as calibration and measurement data are available from:

<http://people.csail.mit.edu/jaffer/convect>

## 17. References

- [1] V Lienhard, John H. Heat Transfer in Flat-Plate Boundary Layers: A Correlation for Laminar, Transitional, and Turbulent Flow. *Journal of Heat Transfer*, 142(6), 04 2020, doi:10.1115/1.4046795. 061805.
- [2] Aubrey Jaffer. Skin-friction and forced convection from rough and smooth plates. *Thermo*, 3(4):711–775, 2023, doi:10.3390/thermo3040040.
- [3] Tetsu Fujii and Hideaki Imura. Natural-convection heat transfer from a plate with arbitrary inclination. *International Journal of Heat and Mass Transfer*, 15(4):755–764, 1972, doi:10.1016/0017-9310(72)90118-4.
- [4] Stuart W Churchill and Humbert HS Chu. Correlating equations for laminar and turbulent free convection from a vertical plate. *International journal of heat and mass transfer*, 18(11):1323–1329, 1975, doi:10.1016/0017-9310(75)90243-4.
- [5] Aubrey Jaffer. Natural convection heat transfer from an isothermal plate. *Thermo*, 3(1):148–175, 2023, doi:10.3390/thermo3010010.
- [6] S. W. Churchill and R. Usagi. A general expression for the correlation of rates of transfer and other phenomena. *AIChE Journal*, 18(6):1121–1128, 1972, doi:10.1002/aic.690180606.
- [7] Hermann Schlichting. *Boundary-Layer Theory*. McGraw Hill, New Delhi, seventh edition, 2014. Translated by Kestin, J.
- [8] C.A. Hieber. Mixed convection above a heated horizontal surface. *International Journal of Heat and Mass Transfer*, 16(4):769–785, 1973, doi:https://doi.org/10.1016/0017-9310(73)90090-2.
- [9] X. A. Wang. An experimental study of mixed, forced, and free convection heat transfer from a horizontal flat plate to air. *Journal of Heat Transfer*, 104(1):139–144, 1982, doi:10.1115/1.3245040.
- [10] D L Siebers, R G Schwind, and R J Moffat. Experimental mixed-convection heat transfer from a large, vertical surface in a horizontal flow. Technical report, Sandia National Lab., Livermore, CA (United States), 7 1983.
- [11] N. Ramachandran, B. F. Armaly, and T. S. Chen. Measurements and Predictions of Laminar Mixed Convection Flow Adjacent to a Vertical Surface. *Journal of Heat Transfer*, 107(3):636–641, 08 1985, doi:10.1115/1.3247471.
- [12] HT Lin, WS Yu, and CC Chen. Comprehensive correlations for laminar mixed convection on vertical and horizontal flat plates. *Wärme-und Stoffübertragung*, 25(6):353–359, 1990.
- [13] C.J. Kobus and G.L. Wedekind. An experimental investigation into forced, natural and combined forced and natural convective heat transfer from stationary isothermal circular disks. *International Journal of Heat and Mass Transfer*, 38(18):3329 – 3339, 1995, doi:10.1016/0017-9310(95)00096-R.
- [14] C.J. Kobus and G.L. Wedekind. An experimental investigation into natural convection heat transfer from horizontal isothermal circular disks. *International Journal of Heat and Mass Transfer*, 44(17):3381 – 3384, 2001, doi:10.1016/S0017-9310(00)00330-6.
- [15] F.B. Rowley, A.B. Algren, and J.L. Blackshaw. Surface conductances as affected by air velocity, temperature and character of surface. *ASHVE Trans.*, 36:429–446, 1930.
- [16] F.P. Incropera, D.P. DeWitt, T.L. Bergman, and A.S. Lavine. *Fundamentals of Heat and Mass Transfer*. Wiley, Hoboken, NJ, USA, 2007.
- [17] T Aihara, Y Yamada, and S Endö. Free convection along the downward-facing surface of a heated horizontal plate. *International Journal of Heat and Mass Transfer*, 15(12):2535 – 2549, 1972, doi:10.1016/0017-9310(72)90145-7.
- [18] A. Žukauskas and A. Šlančiauskas. *Heat Transfer in Turbulent Fluid Flows*. Hemisphere Publishing Corp, Washington, DC, 1987.

- [19] J. H. Lienhard, IV and J. H. Lienhard, V. *A Heat Transfer Textbook*. Phlogiston Press, Cambridge, MA, 5th edition, August 2020. Version 5.10.
- [20] R.W. Rice. Emittance factors for infrared thermometers used for wood products. *Wood and Fiber Science*, 36:520–526, 2004.
- [21] Eva Barreira, Ricardo M. S. F. Almeida, and Maria L. Simes. Emissivity of building materials for infrared measurements. *Sensors*, 21(6), 2021, doi:10.3390/s21061961.
- [22] R.B. Abernethy, R.P. Benedict, and R.B. Dowdell. Asme measurement uncertainty. *ASME. J. Fluids Eng.*, 107(2):161–164, 1985, doi:10.1115/1.3242450.